

Localized wave physics and engineering

Richard W. Ziolkowski*

*Electromagnetics Laboratory, Department of Electrical and Computer Engineering, Building 104, Room 422E,
University of Arizona, Tucson, Arizona 85721*

(Received 12 December 1990; revised manuscript received 29 April 1991)

Issues pertaining to the rate of beam divergence, the beam intensity, and the measured energy efficiency of beams generated by arrays of radiating elements are central to the practical applications of those beams. It will be shown that a localized-wave pulse-driven array can be designed to outperform similar continuous-wave pulse-driven arrays with respect to each of these beam characteristics. This improved performance is quantified by deriving bounds on those beam quantities for the field generated by an arbitrary pulse-driven array. These bounds extend the meaning of near-field distances or diffraction lengths to the situation where the array driving functions can be broad-bandwidth signals. Particular attention is given to transmitting- and receiving-array systems consisting of elements that are not large in comparison to the shortest wavelength of significance contained in the signals driving them. The output signals of such systems are related to the input driving functions by several time derivatives. It is demonstrated that the properties of the resulting beams depend on the higher-order moments of the spectra of the input driving functions and that diffraction degrades the coherence of these higher-order moments more slowly than its lower orders. A properly designed set of input driving signals having a high degree of correlation in the higher-order moments of their spectra will produce a beam that has extended diffraction lengths and localization properties. The localized-wave solutions provide an immediate access to this situation. An alternative type of array is required to realize these localized-wave effects—one that has independently addressable elements. The enhanced localization effects are then intimately coupled to the proper spatial distribution of broad-bandwidth signals driving the array, i.e., by controlling not only the amplitudes, but also the frequency spectra of the pulse driving the array. Recently reported experimental comparisons between localized-wave and continuous-wave pulse-driven arrays of ultrasonic transducers in water are reexamined in terms of the theoretical developments presented here. It will be shown that the observed performance enhancements of the localized-wave pulse-driven arrays are in agreement with the theoretical predictions.

I. INTRODUCTION

Large classes of more-or-less localized space-time solutions to the equations governing many wave phenomena (e.g., scalar wave [1–6], Maxwell's [3,7], Klein-Gordon [8] equations) have been reported recently. When compared with traditional monochromatic, continuous-wave (CW) solutions such as Gaussian or piston beams, these localized-wave (LW) solutions are characterized by extended regions of localization; i.e., their shapes and/or amplitudes are maintained over much larger distances than their CW analogs. Also, they cannot be written as the product of a function only of time and a function only of space; i.e., the LW solutions are mathematically nonseparable in the space-time coordinates. These discoveries have prompted several extensive investigations into the possibility of using these LW solutions to drive finite-size arrays and thus to launch fields having extended localization properties.

The physics behind the LW effect involves array elements driven with broad-bandwidth signals whose time dependence varies from location to location. This scheme exploits an additional degree of freedom not used with current CW systems: a designed union between the space and frequency portions of phase space. A LW solution naturally provides this connection; the spatially dis-

tributed component wave forms and, therefore, their broad-bandwidth spectra are correlated to each other, a self-similarity property inherent in a LW solution. The degree of these correlations can be optimized for a given system. Away from the array the dependence of the current spectrum on location follows from different spectral contributions to the pulse arriving from different locations. A moving interference pattern forms at enhanced distances as the individual wave forms continue to propagate away from their sources. An alternative type of array is necessary to achieve this effect—each array element must be independently addressable so that the appropriate broad-bandwidth time signal can be radiated from it. This is in contrast to conventional arrays that deliver the same CW or narrow-bandwidth time signal to each subsystem and then only have independent phase control over each radiating element for beam-steering purposes and amplitude control (shading) for the setting of sidelobe levels. Enhanced localization effects can be achieved by driving an array with a properly designed spatial distribution of broad-bandwidth signals; i.e., by shading not only the amplitudes, but also the frequency spectra of the pulses driving the array. Evidence confirming this LW effect with ultrasonic waves in water has been reported [9,10].

Even with experimental confirmation of these con-

cepts, several issues need further clarification, particularly the claimed ability of a beam generated by a LW pulse-driven array to outperform one generated by a CW pulse-driven array. Several arguments [11,12] have been raised that theoretically question the possibility of constructing an array that is more efficient than a conventional CW pulse-driven array. These also bring into question some of the experimental results, because of possible ambiguities that might exist in the choices of the lengths and frequencies used to make the comparisons between the LW and CW pulse-driven arrays. These performance comparisons are desirable and inevitable.

Meaningful comparisons of broadband and narrow-band array performance are difficult. The LW solutions are composed of broad-bandwidth wave forms while traditional performance criteria such as the beam divergence, beam intensity, and measured beam energy are based upon CW or, at most, narrow-bandwidth concepts. There is no apparent special frequency that can be chosen in a traditional manner to define, for instance, a near-field (Rayleigh) distance or diffraction length when several different broad-bandwidth spectra are involved. Moreover, it is found that those beam quantities are connected with different portions of the frequency spectra in the broad-bandwidth case, a possibility that does not arise in the CW problem.

In this paper performance bounds on the quantities associated with a beam generated by an arbitrary pulse-driven array, e.g., beam divergence, transmitted beam intensity, and measured beam energy, are derived analytically. In particular, the concept of a Rayleigh distance or diffraction length is extended from the narrow-bandwidth case to a broad-bandwidth configuration. This generalization will require the introduction of a frequency value that is characteristic of the frequencies associated with each beam quantity under investigation. It will be shown that there exist natural choices for these characteristic frequency values. Comparisons of these values with more conventional choices will also be considered. The existence of these characteristic frequencies is very important, since it will permit a well-defined comparison between the efficiencies and the spreading of the beams generated by a CW and a LW pulse-driven array.

Particular attention will be given to transmitting and receiving systems whose elements are not large in comparison to the shortest wavelength of significance contained in the time domain signals driving them. The ultrasonic transducers used in the experiments reported in Refs. [9] and [10] as well as many electromagnetic systems [13], satisfy this condition. A direct consequence of this condition is that the output signals are related by several time derivatives to the input driving functions. A model acoustic-transducer transmitting and receiving system is given in Appendix A to quantify this point. It will be shown that the bounds on the beam properties of the fields associated with such a system can be characterized by the higher-order moments of the spectra of the input driving functions. Derivatives of signals are generally thought to be a nuisance in real systems because they tend to degrade the signal-to-noise ratio. These beam property bounds indicate that this need not be the case.

The diffraction length associated with the efficiency of the field generated by an array of radiating elements driven with a single CW signal is characterized by the area of that array divided by the wavelength of the signal driving it. The transverse pattern, hence, spread of this beam is characterized by the phase coherence between signals originating from different locations in the array. The rate of divergence of the mainlobe of this beam is related to the wavelength divided by the characteristic length of the array. Thus by linear superposition, if each element in an array is driven with the same short time signal (broad-bandwidth pulse), the lower-frequency components of the resulting beam will diffract more quickly than its higher-frequency components and the interference of these successively diffracting frequency-field components will form the pattern. These frequency shedding and interference properties are intrinsic to the diffraction process. The bounds presented below naturally extend these characterizations to the cases where the array is driven with an arbitrary spatial distribution of broad-bandwidth signals and where the transmitting and receiving systems bestow higher-order time derivatives onto the signals. It will be shown that the diffraction process degrades the higher-order space-time correlation properties of a beam more slowly than its lower-order properties. Thus, with a set of input driving signals properly tailored to the actual transmitter-receiver-array system, i.e., a set of signals designed to have a high degree of correlation in the higher-order moments of their spectra, one can produce a beam that has enhanced localization properties. Numerical results supporting these arguments will be given; the experimental results will be reevaluated in terms of these bounds. The reported conclusion [10] that a LW pulse-driven array can outperform its CW counterpart is reaffirmed by this investigation.

Contained within these physics arguments in the engineering issue of how to maximize the performance of a finite array, i.e., how one can achieve the upper limits of the bounds in practice. If one could launch, for instance, one of the LW general source-free solutions of the scalar wave equation from an acoustic array, one would be able to achieve enormous performance enhancements. However, can such a beam be realized? If not, can signals other than the LW solutions or modifications of them be used to achieve further performance gains? Several potential methods for defining the array driving functions are available and will be considered. Their efficiency in regard to generating a beam with enhanced localization properties will be discussed and supported with numerical examples. In contrast to this analysis approach, a source-synthesis technique was considered in Ref. [14]. The array and the desired field were specified, and an inverse problem was solved to find a set of input driving signals that would produce a best estimate of the desired field in the presence of all the wave-diffraction and wave-interference effects. Although this optimization approach achieves the desired beam-localization effects, it does not reveal answers to the basic questions considered here.

In Sec. II, the issues of beam divergence, transmitted beam intensity, and measured beam energy will be ad-

ressed for arbitrary pulse-driven array. The presentation will focus on the acoustic, scalar case. This will simplify the discussion and will permit a further explanation of the experimental results obtained to date. Extensions to the electromagnetic case are straightforward and have been considered elsewhere [13]. Numerical examples will be given in Sec. III to characterize these arguments relative to their impact on generating a beam that exhibits the desired enhanced localization effects. In particular, it will be demonstrated explicitly that a set of LW signals can be designed for a pulse-driven array so that it will generate a beam which will outperform its CW counterpart in a variety of applications. In Sec. IV we briefly review and summarize the physics and engineering issues presented here.

II. BEAM DIVERGENCE AND ENERGY EFFICIENCY

First, consider Fig. 1. It is assumed that one has an array of N independently addressable radiating elements, such as ultrasonic transducers in water, that are arbitrarily located in space. Each element is assumed to have the radiating area A_j associated with it and is excited with the driving function $f_j(t)$. The total radiating area A of the array is

$$A = \sum_{j=1}^N A_j . \quad (2.1)$$

The only constraint on the driving functions is that they be continuous. The associated frequency spectra will be labeled $F_j(\omega)$.

Next, consider a system that consists of a transmitting array of like elements and a similar receiving array in a medium that is isotropic, homogeneous, and frequency independent. Since this system is linear, it can be characterized by the behavior of a unit pair of transmitting and receiving elements. This behavior is described in Appendix A for array elements that are not large in comparison to the shortest wavelength of significance contained in the time domain signals driving them, i.e., their characteristic length l and this wavelength λ_{\min} satisfy

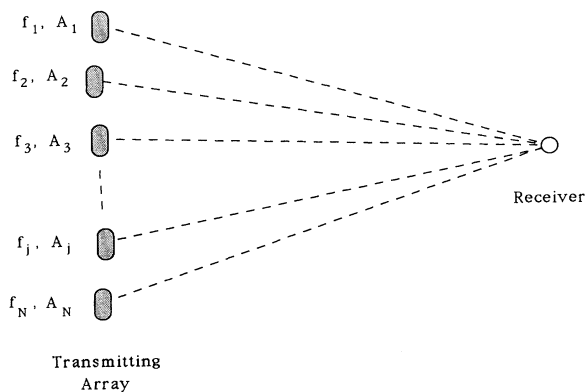


FIG. 1. The received signal is a combination of pulses radiated from each element in the array.

$2\pi l / \lambda_{\min} = k_{\max} l \lesssim 1$, and that are driven far from their resonance frequencies. The ultrasonic transducers (e.g., small piezoelectric disks) used in the experiments reported in Refs. [9] and [10] satisfy these conditions; analogous electromagnetic systems consist of electrically short dipole antennas [13]. As shown in Appendix A, the output signals measured at the receiver elements in such a system are related by three time derivatives to the input signals driving the transmitting elements. The first time derivative results from the conversion of the electrical energy fed to the transducer into field energy near it; the second one from the radiation process which converts (propagates) this near-field energy into field energy far from the radiator; and the third one, by reciprocity, results from the conversion of the field energy into electrical energy in the transducer. This three-time-derivative behavior was reported by Cook and Lewis in Ref. [15] and is confirmed by the experimental results [9,10]. When the array elements are large in comparison to the shortest wavelength of significance: $k_{\max} l \gg 1$, they usually have little effect on the signals during the energy conversion processes, and the output signal is simply proportional to the one time derivative of the input signal resulting from the radiation process. Other behaviors are possible [13]; our discussion will focus on the behavior of these two basic models of the acoustic-transducer transmitting and receiving systems. Their properties are summarized in Fig. 2.

In order to simplify the discussion, several field classifications are introduced. The set of driving functions $\{f_j\}_{j=1, \dots, N}$ constitute the *input field*. This situation is analogous to driving an aperture with a space-time beam, hence the name. The units of an input signal f_j are taken to be $(\text{W}/\text{m}^2)^{1/2}$. The radiating elements, such as the ultrasonic transducers in water or electric dipoles in air, take this input field and create the *radiated field*. In the case that $k_{\max} l \lesssim 1$ this represents the field near the radiating element; in the case that $k_{\max} l \gg 1$ it is the field far from it. A representation of the field generated from a planar aperture of finite area A_n normal to the z direction is given by [16]

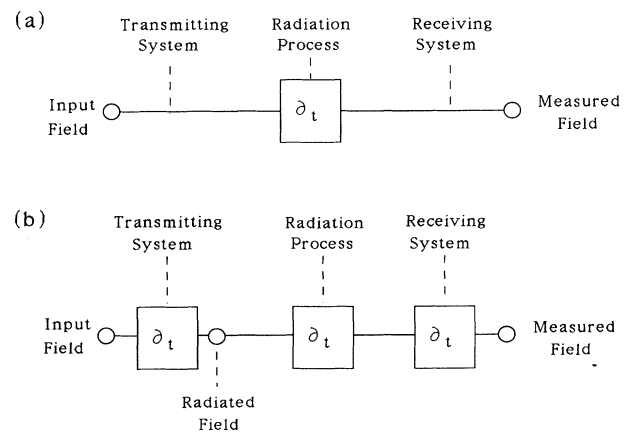


FIG. 2. The relationships between the input, radiated, and measured fields: (a) when $k_{\max} l \gg 1$, and (b) when $k_{\max} l \lesssim 1$.

$$g(\mathbf{r}, t) = \int_{A_n} dS' \Psi(x', y', z', t - R/c) \frac{1}{4\pi R}, \quad (2.2a)$$

where $R = |\mathbf{r} - \mathbf{r}'|$ and the term

$$\begin{aligned} \Psi(x', y', z', t - R/c) = & -[\partial_{z'} f] + [\partial_{ct'} f] \frac{(z - z')}{R} \\ & + [f] \frac{(z - z')}{R^2}. \end{aligned} \quad (2.2b)$$

All quantities in square brackets in (2.2b) are evaluated at the indicated retarded time. The expressions (2.2) represent an approximation of Huygens's representation of the field to the right of an infinite plane $z' = \text{const}$. This Kirchhoff approximation, as it is called, assumes that the initial field distribution is zero everywhere in that plane except over A_n . The z -plane constant is determined by the requirement that the field and its time derivative be zero on this plane at $t = 0$. In practice the initial time can be adjusted so that any $z' = \text{const}$ plane can be utilized. For all of the efficiency calculations to be presented below, only the field generated along the axis of the array will be considered. It is assumed that the elements are distributed arbitrarily, but in a fashion so that this axis is reasonably well defined. For a finite number N of radiating elements, the field (2.2a) can be approximately written as

$$g(\mathbf{r}, t) \simeq \sum_{n=1}^N \frac{\Psi_n(\mathbf{r}_n, t - |\mathbf{r} - \mathbf{r}_n|/c) A_n}{4\pi |\mathbf{r} - \mathbf{r}_n|}, \quad (2.2c)$$

where the \mathbf{r}_n , $n = 1, 2, \dots, N$, are the locations of the elements in the array and $\Psi_n(\mathbf{r}_n, t) \equiv \Psi(\mathbf{r}_n, t)$. Then, assuming that the characteristic length associated with an individual element is much smaller than the distance of observation from the array, one has $R \sim (z - z')$ so that $\Psi(x', y', z', t) \sim 2\partial_{ct'} f$. Therefore the expression for the field radiated from the n th element at \mathbf{r}_n to a point in space-time (\mathbf{r}, t) spatially far from the array reduces to the simple form

$$g_n^{\text{rad}}(\mathbf{r}, t) \sim \frac{A_n}{2\pi c |\mathbf{r} - \mathbf{r}_n|} \partial_t f_n(\mathbf{r}_n, t - |\mathbf{r} - \mathbf{r}_n|/c). \quad (2.3a)$$

Consequently, the total *radiated field* from the array to such a point is

$$g_{\text{rad}}(\mathbf{r}, t) \sim \sum_{n=1}^N \frac{A_n}{2\pi c |\mathbf{r} - \mathbf{r}_n|} \partial_t f_n(\mathbf{r}_n, t - |\mathbf{r} - \mathbf{r}_n|/c). \quad (2.3b)$$

Note that this model does not include the spatial pattern of each radiating element (the effects of the actual distribution of the fields across the area associated with each element) nor the coupling to adjacent elements. It assumes that the field radiated by *each* element of the array has reduced to the field radiated by a point source before it reaches the location of the receiver. If a more accurate value of the field is required, one must resort to the more complete calculation given by (2.2c).

Again referring to Fig. 2, the radiated field is not the same as the measured field when $k_{\text{max}} l \lesssim 1$. One must take into account the time derivative introduced by the

receiver-detector during the measurement of the field (i.e., its frequency response) as well as the time derivative introduced by its propagation from the transmitter to the receiver. The medium assumed here does not impact the beam during propagation; in general one must also account for the frequency properties of the medium during this propagation phase. Note that this transition from the radiated to measured fields in no way influences the behavior of the source or the input field or the radiated field. Thus the *measured field* at a point in space-time generated by an array of small acoustic disk transducers has the form

$$g_{\text{meas}}(\mathbf{r}, t) \simeq \mathcal{C} \partial_t^2 \sum_{n=1}^N \frac{\Psi_n(\mathbf{r}_n, t - |\mathbf{r} - \mathbf{r}_n|/c) A_n}{4\pi |\mathbf{r} - \mathbf{r}_n|}, \quad (2.4a)$$

which at a point spatially far from the array reduces to the simple expression

$$g_{\text{meas}}(\mathbf{r}, t) \sim \mathcal{C} \sum_{n=1}^N \frac{A_n}{2\pi c |\mathbf{r} - \mathbf{r}_n|} \partial_t^3 f_n(\mathbf{r}_n, t - |\mathbf{r} - \mathbf{r}_n|/c). \quad (2.4b)$$

The constant \mathcal{C} has units s^2 and is introduced by the conversion from the radiated to the measured fields. It is model dependent and is defined explicitly in Appendix A for the acoustic-transducer pair. A similar constant that is introduced by the conversion of the actual input time signal into the radiated field has been absorbed into each of the input signals f_n . These constants do not affect any comparisons between the LW and CW pulse-driven arrays since they appear in both cases, being intrinsic to the overall system. Similar results are obtained for an analogous system of electrically small dipole antennas [13].

Note that in the CW case, the input, radiated, and measured fields are simply related by powers of the frequency, a single constant. There is essentially no difference between the radiated, propagated, and measured fields, so this issue does not arise even if there is spatial variation in the field. However, in the LW case, the energy-conversion effects must be taken into account. The arriving time signals are spatially distributed, each bringing to a transmitting or receiving element a different broad-bandwidth spectrum. Because of the different time derivatives involved, different portions of the frequency spectra of those signals will control the associated beam characteristics.

The transmitted-energy efficiency is usually quoted as a performance rating for a source like an acoustic array. This efficiency should simply be a ratio of the received energy to the input energy. Therefore a connection must be made between the functions' input into the array to drive it and the received signals. However, this is but one characteristic of a beam launched from a pulse-driven array. Several other performance criteria are possible and must be considered. The arguments that will be discussed below deal with various definitions of the array efficiency that require the intensities and energies of the various fields involved in the transmitted, propagated, and measured beam fields.

If the observation point is spatially located along the

axis of the array at $\mathbf{r}=(0,0,z)$ and $R_j=|\mathbf{r}-\mathbf{r}_j|$, the intensities and energies that will be needed in the following discussion are given by the following expressions (units for each are given in parentheses).

Input-field energy (J):

$$\mathcal{E}_{\text{in}} = \sum_{n=1}^N A_n \int_{-\infty}^{\infty} dt |f_n(\mathbf{r}_n, t)|^2 = \sum_{n=1}^N \mathcal{E}_n^{\text{in}}. \quad (2.5)$$

Radiated-field (near-field) intensity (W/m²):

$$\mathcal{J}_{\text{rad}}(\mathbf{r}, t) = \left| \sum_{n=1}^N A_n \frac{\Psi_n(\mathbf{r}_n, t - R_n/c)}{4\pi R_n} \right|^2. \quad (2.6a)$$

Radiated-field (near-field) fluence (J/m²):

$$\begin{aligned} \mathcal{F}_{\text{rad}}(\mathbf{r}) &= \int_{-\infty}^{\infty} dt \mathcal{J}_{\text{rad}}(\mathbf{r}, t) \\ &= \int_{-\infty}^{\infty} dt \left| \sum_{n=1}^N A_n \frac{\Psi_n(\mathbf{r}_n, t - R_n/c)}{4\pi R_n} \right|^2. \end{aligned} \quad (2.6b)$$

Radiated-field (far-field) intensity (W/m²):

$$\mathcal{J}_{\text{rad}}(\mathbf{r}, t) = \left| \sum_{n=1}^N A_n \frac{\partial_t f_n(\mathbf{r}_n, t - R_n/c)}{2\pi c R_n} \right|^2. \quad (2.7a)$$

Radiated-field (far-field) fluence (J/m²):

$$\mathcal{F}_{\text{rad}}(\mathbf{r}) = \int_{-\infty}^{\infty} dt \left| \sum_{n=1}^N A_n \frac{\partial_t f_n(\mathbf{r}_n, t - R_n/c)}{2\pi c R_n} \right|^2. \quad (2.7b)$$

Measured-field (far-field) intensity (W/m²):

$$\mathcal{J}_{\text{meas}}(\mathbf{r}, t) = \mathcal{E}^2 \left| \sum_{n=1}^N A_n \frac{\partial_t^3 f_n(\mathbf{r}_n, t - R_n/c)}{2\pi c R_n} \right|^2. \quad (2.8a)$$

Measured-field (far-field) fluence (J/m²):

$$\begin{aligned} \mathcal{F}_{\text{meas}}(\mathbf{r}) &= \int_{-\infty}^{\infty} dt \mathcal{J}_{\text{meas}}(\mathbf{r}, t) \\ &= \mathcal{E}^2 \int_{-\infty}^{\infty} dt \left| \sum_{n=1}^N A_n \frac{\partial_t^3 f_n(\mathbf{r}_n, t - R_n/c)}{2\pi c R_n} \right|^2. \end{aligned} \quad (2.8b)$$

Note that the terms ‘‘far field’’ and ‘‘near field’’ refer here simply to whether the observation point is or is not spa-

tially far from the array so that the approximation $\Psi_n \simeq 2\partial_{ct} f_n$ is or is not valid. The normal use of these terms is defined by the Rayleigh distance; this terminology is extended to the general broad-bandwidth case after the derivations given below.

The input-field energy is the energy distributed to the array from some power source, the n th element receiving $\mathcal{E}_n^{\text{in}}$ J. Because the radiated and measured fields are observed at a single point rather than over an area, their fluences, essentially an average energy per unit area, will be considered. The input fluence is given simply as

$$\mathcal{F}_{\text{in}} = \frac{\mathcal{E}_{\text{in}}}{A}, \quad (2.9)$$

where A is the total area of the radiating array given by (2.1). To avoid the introduction of fluences, one could equally well consider the energy received over a unit area. In the case of a uniformly spaced, planar array, this choice is possible since a unit area is readily available. This is not the case in general and the fluence concept becomes an appropriate quantity to investigate.

A. Radiated-field bound

Consider first the efficiency defined by the ratio of the radiated-field energy to the input field energy:

$$\Gamma_{\text{rad}} = \frac{\mathcal{F}_{\text{rad}}}{\mathcal{F}_{\text{in}}}. \quad (2.10)$$

This is a measure of how much energy is radiated away from the array. From (2.7b) the radiated fluence in the far field can be written explicitly as

$$\mathcal{F}_{\text{rad}}(\mathbf{r}) = \left[\frac{1}{2\pi c} \right]^2 \sum_{m=1}^N \sum_{n=1}^N \frac{A_m^{1/2} A_n^{1/2}}{R_m R_n} \Lambda_{mn}^{\text{rad}} \mathcal{U}_m^{1/2} \mathcal{U}_n^{1/2}, \quad (2.11)$$

where the radiated far-field energy term

$$\mathcal{U}_n = A_n \int_{-\infty}^{\infty} dt |\partial_t f_n(\mathbf{r}_n, t)|^2 \quad (2.12)$$

and the correlations of the radiated signals are measured by the quantity

$$\Lambda_{mn}^{\text{rad}}(\mathbf{r}) = \frac{\int_{-\infty}^{\infty} dt \partial_t f_m(\mathbf{r}_m, t - R_m/c) \partial_t f_n(\mathbf{r}_n, t - R_n/c)}{\left[\int_{-\infty}^{\infty} dt |\partial_t f_m(\mathbf{r}_m, t)|^2 \right]^{1/2} \left[\int_{-\infty}^{\infty} dt |\partial_t f_n(\mathbf{r}_n, t)|^2 \right]^{1/2}}. \quad (2.13)$$

First note that the Schwarz inequality [17] requires

$$\Lambda_{mn}^{\text{rad}} \leq 1. \quad (2.14)$$

Since the product $R_m R_n$ accounts for the $1/r^2$ decay of the energy, a set of drive functions $\{f_n\}$ whose correlation functions $\Lambda_{mn}^{\text{rad}}$ increase as the range increases can maintain the radiated-field efficiency. This is also indicative of an enhanced beam-divergence behavior: the beam quality must be maintained to promote the enhanced radiated-field energy. However, because (2.14) must be

satisfied, the distance over which this effect can be accomplished is limited. Combining (2.11) and (2.14), one has

$$\begin{aligned} \mathcal{F}_{\text{rad}}(\mathbf{r}) &\leq \left[\frac{1}{2\pi c} \right]^2 \left[\sum_{n=1}^N \frac{\mathcal{U}_n^{1/2} A_n^{1/2}}{R_n} \right]^2 \\ &\leq \left[\frac{1}{2\pi c} \right]^2 \sum_{n=1}^N \frac{\mathcal{U}_n}{R_n^2} \sum_{m=1}^N A_m = A \left[\frac{1}{2\pi c} \right]^2 \sum_{n=1}^N \frac{\mathcal{U}_n}{R_n^2}, \end{aligned} \quad (2.15)$$

where the Schwarz inequality has been invoked again to obtain the last expression.

Now locate all of the sources on the plane $z=0$. As noted above, this assumption does not detract from the generality of the arguments. Since for any element $R_n \geq z$, Eq. (2.15) reduces in this case to the form

$$\mathcal{F}_{\text{rad}}(\mathbf{r}) \leq \left[\frac{A}{2\pi cz} \right]^2 \frac{\mathcal{U}_{\text{rad}}}{A}, \quad (2.16a)$$

where the total radiated-field energy

$$\mathcal{U}_{\text{rad}} = \sum_{n=1}^N \mathcal{U}_n. \quad (2.16b)$$

Also let each of the sources have the same area $A_n = A_0$ so that $A = NA_0$. In the CW case let each element of the array be driven with the same CW signal having the angular frequency ω_{CW} so that $\int dt |\partial_t f|^2 = \omega_{\text{CW}}^2 \int dt |f|^2$. This means that the input- and radiated-energy-density terms are the same for each element: $\mathcal{E}_n^{\text{in}} = \mathcal{E}_0^{\text{in}}$ and $\mathcal{U}_n = \mathcal{U}_0 \equiv \omega_{\text{CW}}^2 \mathcal{E}_0^{\text{in}}$. Therefore in the CW case one has the input- and radiated-field fluences

$$\mathcal{F}_{\text{in}}^{\text{CW}} = \frac{\mathcal{E}_0^{\text{in}}}{A_0}, \quad (2.17a)$$

$$\mathcal{F}_{\text{rad}}^{\text{CW}}(\mathbf{r}) \leq \left[\frac{A}{2\pi cz} \right]^2 \frac{\mathcal{U}_0}{A_0}, \quad (2.17b)$$

which yield the CW radiated far-field efficiency:

$$\Gamma_{\text{rad}}^{\text{CW}} \leq N^2 \left[\frac{A_0}{\lambda_{\text{CW}} z} \right]^2 \equiv \left[\frac{A}{\lambda_{\text{CW}} z} \right]^2 = \left[\frac{L_{\text{CW}}}{z} \right]^2, \quad (2.17c)$$

where $\omega_{\text{CW}}/c = k_{\text{CW}} = 2\pi/\lambda_{\text{CW}}$ and the Rayleigh distance or diffraction length associated with the radiated CW field energy $L_{\text{CW}} = A/\lambda_{\text{CW}}$ has been introduced. The CW radiated efficiency is thus bounded by the coherent superposition of all of the radiating elements. This result recovers the so-called ‘‘antenna theorem’’ [18].

Now consider the far-field efficiency for the same set of radiating elements but with a set of LW driving functions. One has

$$\Gamma_{\text{rad}}^{\text{LW}} \leq \left[\frac{A}{2\pi cz} \right]^2 \frac{\mathcal{U}_{\text{rad}}^{\text{LW}}}{\mathcal{E}_{\text{in}}^{\text{LW}}}. \quad (2.18)$$

Recall that functions like the LW's consist of broad-bandwidth components. To provide a quantitative measure of the frequencies involved in these signals, let us introduce an ‘‘effective frequency’’ of the radiated near fields, Ω_{rad} , and far fields, ω_{rad} . In particular, set

$$\begin{aligned} \Omega_{\text{rad}}^2 &= \frac{\mathcal{U}_{\text{rad}}^{\text{LW}}(\text{near field})}{\mathcal{E}_{\text{in}}^{\text{LW}}} \\ &= \frac{\sum_{n=1}^N A_n \int_{-\infty}^{\infty} dt |\Psi_n(\mathbf{r}_n, t)|^2}{\sum_{n=1}^N A_n \int_{-\infty}^{\infty} dt \left| \int_{-\infty}^{\infty} dt \Psi_n(\mathbf{r}_n, t) \right|^2}, \end{aligned} \quad (2.19a)$$

$$\begin{aligned} \omega_{\text{rad}}^2 &= \frac{\mathcal{U}_{\text{rad}}^{\text{LW}}(\text{far field})}{\mathcal{E}_{\text{in}}^{\text{LW}}} \\ &= \frac{\sum_{n=1}^N A_n \int_{-\infty}^{\infty} dt |\partial_t f_n(\mathbf{r}_n, t)|^2}{\sum_{n=1}^N A_n \int_{-\infty}^{\infty} dt |f_n(\mathbf{r}_n, t)|^2} \\ &= \frac{\sum_{n=1}^N A_n \int_{-\infty}^{\infty} d\omega \omega^2 |F_n(\mathbf{r}_n, \omega)|^2}{\sum_{n=1}^N A_n \int_{-\infty}^{\infty} d\omega |F_n(\mathbf{r}_n, \omega)|^2}. \end{aligned} \quad (2.19b)$$

The near-field (far-field) effective frequency measures the frequency content of the fields launched from the array into the medium near (far from) that array. The efficiency (2.18) can now be rewritten simply as

$$\Gamma_{\text{rad}}^{\text{LW}} \leq \left[\frac{A}{\lambda_{\text{rad}} z} \right]^2 = \left[\frac{L_{\text{rad}}}{z} \right]^2, \quad (2.20)$$

where the wavelength $\lambda_{\text{rad}} = 2\pi c/\omega_{\text{rad}}$ and the Rayleigh distance associated with the radiated-field energy $L_{\text{rad}} = A/\lambda_{\text{rad}}$ has been introduced. The derivation of (2.20), which is accomplished without any plane-wave assumptions, is a generalization of the so-called ‘‘brightness theorem’’ derived in Ref. [11]. The arguments in Ref. [11] center about the relation

$$\frac{\Gamma_{\text{rad}}^{\text{LW}}}{\Gamma_{\text{rad}}^{\text{CW}}} \sim \left[\frac{\omega_{\text{rad}}}{\omega_{\text{CW}}} \right]^2, \quad (2.21)$$

and whether this ratio can be greater or less than 1. It is argued that that one can always achieve a source with $\omega_{\text{CW}} = \omega_{\text{rad}}$ making this ratio always less than one, hence making the LW case at most as efficient as the corresponding CW case. This argument misses several important points.

First and foremost, even though the radiated and measured fields are related by a constant in the CW case, they are not in the LW case. Hence the ratio (2.21) does not correctly define the measured energy efficiency of the array. It does not account for the measurement process. The radiated field, like a potential, has stored energy to do work. However, until a probe is inserted to measure that field, no actual energy of the field is expended.

Second, if one wants to make a fair comparison between the performance of an array driven with a set of LW driving functions rather than a CW set, some realistic measure of the frequencies contained in the LW set must be found. The effective frequency values Ω_{rad} and ω_{rad} are appealing quantities for this purpose. The former is a ratio of the array-weighted accumulation of the contributions to the energy spectrum of the field near the array face and the array-weighted accumulation of the energy spectra of the signals driven into the array. The latter replaces the energy spectrum of the field near the

array face with the energy spectrum of the field far from it. Note that

$$\Omega_{\text{rad}} \leq \omega_{\text{rad}} . \quad (2.22a)$$

This property of the near-field and far-field frequency spectra is associated with the fact that the lower-frequency components are radiated less efficiently into the far field *and* require more energy to excite them. The beam, in essence, can shed its lower frequencies as it propagates. If the input signals and the radiating elements are not designed properly to account for this frequency-shedding property, the beam generated by the array will quickly lose its lower-frequency components as it propagates, resulting in a degradation of the shape of the beam and an ensuing increase in cost of its energy efficiency. One can easily argue that the near-field effective frequency should be the value to which one should assign the CW frequency for any comparisons between the beams generated by LW and CW pulse-driven arrays. It accounts for the spectral energies launched into the medium. However, these effective frequencies do not address an essential difference between the input field and the radiated field. Consider the input set of driving functions. These functions deliver the energy to the array. The electronics driving the array will expend this energy to create these signals, to pass them to the radiating elements, and to radiate them. The driving function spectra have an upper frequency ω_{max} above which they contain very little spectral energy. We have chosen the second e -folding point of the array-weighted energy spectrum (frequency at which this energy spectrum has decreased to $1/e^2$, its maximum value) generally for this value [9,10]. This is an overly restrictive value. The standard engineering criterion would be the “3-dB” point of the composite energy spectrum delivered to the array (provided that the spectrum is low pass beyond this point); i.e., the value $\omega_{\text{max}} = \omega_{3 \text{ dB}}$ is chosen to be the frequency at which the total energy spectrum has decreased to half its value. In terms of comparisons between the LW and the corresponding CW cases, one could just as easily argue that the value ω_{max} dealing strictly with the input signals should be the one used to determine the frequency for the CW case, not the value ω_{rad} which is obtained after the array has modified the signals and the beam has propagated into the far field. The effective frequency value Ω_{rad} at least measures the frequency content near the array and removes the dc components which are not involved in the beam-launching process. Since it accounts for the spectral energies that are launched by the array into the medium, it is a better measure of the frequency content of the driving functions than ω_{rad} is. Making Ω_{rad} the choice for the CW case without further consideration, one could already claim that the LW case produces a beam which is more efficient in transmitting energy than the corresponding CW one:

$$\frac{\Gamma_{\text{rad}}^{\text{LW}}}{\Gamma_{\text{rad}}^{\text{CW}}} \sim \left[\frac{\omega_{\text{rad}}}{\omega_{\text{CW}} = \Omega_{\text{rad}}} \right]^2 \geq 1 . \quad (2.22b)$$

This enhancement of the radiated-energy efficiency in the

LW case is even more pronounced if one were to choose $\omega = \omega_{3 \text{ dB}}$, since quite generally the second moment of a broad-bandwidth spectrum is much higher than its 3-dB point. The issue to be reemphasized here is that one can design input driving functions that maximize the differences between any of these values.

From an engineering point of view, (2.20) explains immediately one approach that one could take to design a set of driving functions to maximize the radiated-field energy. One would try to design functions with as fast a rise time as possible, thereby maximizing their first derivatives, hence, the corresponding ω_{rad} . This is, in essence, the basis of the electromagnetic-missile concept [19]. This, unfortunately, also shows a shortcoming in the bound (2.20). It is trivial to design a set of driving functions that have finite energy but have a discontinuity in their first derivative. The bound is then not meaningful. A step function is one that comes immediately to the mind. Driving the array with a set of such driving functions makes $L_{\text{rad}} = \infty$. It is a well-known fact that driving an array with an infinite-bandwidth signal will result in a beam that remains localized to infinity. In fact, as was derived recently [20], the energy decay of such a beam goes as $1/r$ rather than $1/r^2$. On the other hand, a devil’s advocate would say immediately that an infinite-bandwidth array is not available because of hardware (electronics, etc.) limitations, so that such a case cannot be realized physically. One then returns immediately to having to make a choice as to what frequency one uses for quantitative comparisons.

Another issue of a more practical nature is of major importance. In many applications it is not the signal energy that is the quantity of interest, but rather the intensity delivered to a point in space time. This is particularly true in the case of a scattering application such as sonar or radar. Many of those systems rely simply on the detection of the peak intensity scattered by the target. Another example deals with a microscopic situation. The force a charged particle experiences is related to the instantaneous field strength it experiences, not the average over time. Furthermore, in many weapons applications, the power delivered by the beam is the important quantity, not its energy. For example, in many high-power microwave-effects applications it is the maximum intensity of a pulse that causes an upset in the state of a computer chip, whereas the pulse energy can lead to a thermal mode burnout of the device. It will be shown below that the bandwidth of the signal on the “target” is the quantity that determines the maximum intensity there. This property gives a significant advantage to a LW pulse-driven array over a CW array because of the inherent broad bandwidths of its input signals.

B. Measured-field bound

Consider now the measured field. As noted above, the overall efficiency of the transmitting system should be based on the input- and measured-field energies. We will only consider here the measured-field energy in the re-

gion far enough from the array so that (2.3a) is valid. Obvious adjustments to the associated values near the array can be made directly as was done with the radiated-field values.

The measured-field energy terms in the far field from a single source and from the entire array are given by the expressions

$$\Lambda_{mn}^{\text{meas}}(\mathbf{r}) = \frac{\int_{-\infty}^{\infty} dt \partial_t^3 f_m(\mathbf{r}_m, t - R_m/c) \partial_t^3 f_n(\mathbf{r}_n, t - R_n/c)}{\left[\int_{-\infty}^{\infty} dt |\partial_t^3 f_m(\mathbf{r}_m, t)|^2 \right]^{1/2} \left[\int_{-\infty}^{\infty} dt |\partial_t^3 f_n(\mathbf{r}_n, t)|^2 \right]^{1/2}}. \quad (2.24)$$

The Schwartz inequality also constrains this measured signal correlation function:

$$\Lambda_{mn}^{\text{meas}} \leq 1. \quad (2.25)$$

Following the above radiated-field arguments, one has immediately that in the case of a planar array

$$\mathcal{F}_{\text{meas}}^{\text{LW}} \leq \mathcal{O}^2 \left(\frac{A}{2\pi cz} \right)^2 \left(\frac{\mathcal{W}_{\text{meas}}^{\text{LW}}}{A} \right), \quad (2.26)$$

and

$$\begin{aligned} \mathcal{F}_{\text{meas}}^{\text{CW}} &\leq \mathcal{O}^2 \left(\frac{A}{2\pi cz} \right)^2 \left(\frac{\mathcal{W}_{\text{meas}}^{\text{CW}}}{A} \right) \\ &\equiv \omega_{\text{CW}}^4 \mathcal{O}^2 \left(\frac{A}{\lambda_{\text{CW}} z} \right)^2 \left(\frac{\mathcal{E}_{\text{in}}^{\text{CW}}}{A} \right). \end{aligned} \quad (2.27)$$

The ratio of the measured-field fluence to the input-field fluence is the quantity that determines the overall efficiency of the transmitting system. This was the choice made in Ref. [10] for comparisons of theory with experiment. Explicitly, this quantity is

$$\Gamma_{\text{meas}} = \frac{\mathcal{F}_{\text{meas}}}{\mathcal{F}_{\text{in}}}. \quad (2.28)$$

Consider again the planar-array case. The efficiency for the CW array becomes

$$\Gamma_{\text{meas}}^{\text{CW}} \leq \omega_{\text{CW}}^4 \mathcal{O}^2 \left(\frac{A}{\lambda_{\text{CW}} z} \right)^2. \quad (2.29)$$

For an observation point in the far field of the LW array, it takes the form

$$\Gamma_{\text{meas}}^{\text{LW}} \leq \omega_{\text{meas}}^4 \mathcal{O}^2 \left(\frac{A}{\lambda_{\text{rad}} z} \right)^2, \quad (2.30)$$

where the effective frequency of the measured far field is

$$\omega_{\text{meas}}^4 = \frac{\sum_{n=1}^N A_n \int_{-\infty}^{\infty} dt |\partial_t^3 f_n(\mathbf{r}_n, t)|^2}{\sum_{n=1}^N A_n \int_{-\infty}^{\infty} dt |\partial_t f_n(\mathbf{r}_n, t)|^2}. \quad (2.31)$$

Clearly, if each driving function f_n were the same CW

$$\mathcal{W}_n = A_n \int_{-\infty}^{\infty} dt |\partial_t^3 f_n(\mathbf{r}_n, t)|^2, \quad (2.23a)$$

$$\mathcal{W}_{\text{meas}} = \sum_{n=1}^N \mathcal{W}_n. \quad (2.23b)$$

The correlation of the far-field measured time signals takes the form

signal, ω_{meas} recovers its frequency. The ratio of the LW and the CW measured-field efficiencies can now be written simply as

$$\frac{\Gamma_{\text{rad}}^{\text{LW}}}{\Gamma_{\text{rad}}^{\text{CW}}} \sim \left(\frac{\omega_{\text{rad}}}{\omega_{\text{CW}}} \right)^2 \left(\frac{\omega_{\text{meas}}}{\omega_{\text{CW}}} \right)^4. \quad (2.32)$$

Therefore the condition for the LW array to be more efficient than the CW array is simply

$$\omega_{\text{meas}}^2 > \frac{\omega_{\text{CW}}^3}{\omega_{\text{rad}}}. \quad (2.33a)$$

If, for example, we now set $\omega_{\text{CW}} = \omega_{\text{rad}}$, the condition for the LW array to be more efficient than the CW array is simply

$$\omega_{\text{meas}} > \omega_{\text{rad}}. \quad (2.33b)$$

As has been demonstrated experimentally [10] and as will be discussed further in the next section, this improvement is readily achieved with a variety of LW solutions and other broad-bandwidth driving signals. In fact, more than an order-of-magnitude increase in the measured-field energies can be achieved.

C. Beam intensities

As discussed above, the maximum field intensity is the quantity of interest for many practical applications. Consider in the far field of the array the radiated-field intensity (2.7a), repeated here for convenience:

$$\mathcal{J}_{\text{rad}}(\mathbf{r}, t) = \left| \sum_{n=1}^N A_n \frac{\partial_t f_n(\mathbf{r}_n, t - R_n/c)}{2\pi c R_n} \right|^2. \quad (2.34)$$

This expression represents the intensity (W/m²) on a target at a given point in space at a given time. Proceeding as in the energy cases, one obtains the relation

$$\mathcal{J}_{\text{rad}}(\mathbf{r}, t) \leq \left(\frac{A}{2\pi cz} \right)^2 \frac{\sum_{n=1}^N A_n |\partial_t f_n(\mathbf{r}_n, t - R_n/c)|^2}{\sum_{n=1}^N A_n}. \quad (2.35)$$

Introducing the input fluence again as the normalization factor yields

$$\frac{\mathcal{J}_{\text{rad}}(\mathbf{r}, t)}{\mathcal{J}_{\text{in}}} \leq \left[\frac{A}{2\pi cz} \right]^2 \frac{\sum_{n=1}^N A_n |\partial_t f_n(\mathbf{r}_n, t - R_n/c)|^2}{\sum_{n=1}^N A_n \int_{-\infty}^{\infty} dt |f_n(\mathbf{r}_n, t)|^2} . \quad (2.36)$$

Note that this expression represents many time values. To reduce it to a more meaningful quantity, we will consider only the maximum of the intensity time history at a given spatial location $\mathcal{J}_{\text{rad}}^{\text{max}}(\mathbf{r})$. This operation will be denoted by \max_t , e.g., $\mathcal{J}_{\text{rad}}^{\text{max}}(\mathbf{r}) = \max_t \mathcal{J}_{\text{rad}}(\mathbf{r}, t)$. This allows one to define an intensity pattern and to discuss the associated side-lobe levels even in the broad-bandwidth case. Introducing the term

$$\Upsilon_{\text{rad}}(\mathbf{r}) = \frac{\max_t \sum_{n=1}^N A_n |\partial_t f_n(\mathbf{r}_n, t)|^2}{\sum_{n=1}^N A_n \int_{-\infty}^{\infty} dt |\partial_t f_n(\mathbf{r}_n, t)|^2} , \quad (2.37a)$$

and noticing that the maximum of a time shifted time signal is bounded by the maximum of that signal without the time shift so that

$$\frac{\max_t \sum_{n=1}^N A_n |\partial_t f_n(\mathbf{r}_n, t - R_n/c)|^2}{\sum_{n=1}^N A_n \int_{-\infty}^{\infty} dt |\partial_t f_n(\mathbf{r}_n, t)|^2} \leq \Upsilon_{\text{rad}}(\mathbf{r}) , \quad (2.37b)$$

the maximum field intensity normalized by the input fluence is

$$\frac{\mathcal{J}_{\text{rad}}^{\text{max}}(\mathbf{r})}{\mathcal{J}_{\text{in}}} \leq \left[\frac{A}{\lambda_{\text{rad}} z} \right]^2 \Upsilon_{\text{rad}}(\mathbf{r}) . \quad (2.38)$$

The term Υ_{rad} is simply the ratio of the maximum of a function to its time-averaged value. In a CW-tone-burst case (finite, time-windowed CW signal), the maximum of the time derivative of the driving function squared is $\omega_{\text{rad}}^2 \equiv \omega_{\text{CW}}^2$ and the energy of that signal is ω_{CW}^2 times half its time record length T_{CW} . Thus the desired ratio in the CW case becomes

$$\Upsilon_{\text{CW}}^{\text{rad}} = \frac{2}{T_{\text{CW}}} . \quad (2.39)$$

Therefore, if one drives the array with a CW signal for a long time, the value of T_{CW} is large and that of $\Upsilon_{\text{CW}}^{\text{rad}}$ is small. In contrast, the LW driving signals all have broad bandwidths, so that one can achieve a very large instantaneous value of the square of the signals with a small average value over a time period comparable to the CW case. Note that even for comparable levels of the derivatives of the input signals, narrow-bandwidth signals must necessarily have larger time record lengths than broad-bandwidth signals. Thus one can design the LW driving functions to obtain

$$\Upsilon_{\text{LW}}^{\text{rad}} \gg \Upsilon_{\text{CW}}^{\text{rad}} , \quad (2.40)$$

and, hence, a much larger instantaneous field intensity

than in the corresponding CW case.

Note that an energy expression represents an average of the signal intensity over time. Because they contain a broad set of frequencies, the peak intensities in a LW beam can be made quite high as noted above. However, because the drive functions defined by a LW solution and, hence, the input field are generally unipolar and because they can persist with low amplitude ‘‘tails’’ over several time periods of the corresponding effective frequency CW signal, this characteristic becomes diminished when the time average is applied. Thus low average energies result in the LW case in contrast to high peak intensities. Consequently, the performance characteristics of a CW beam are favored by energy arguments; and those of a LW beam are favored in intensity comparisons. It will be shown below that a LW beam can be designed to maintain a much higher intensity value in the far field than its CW counterpart.

Similar considerations for the measured-field quantities yield the relation for the maximum measured-field intensity normalized by the input fluence. This ratio is simply

$$\frac{\mathcal{J}_{\text{meas}}^{\text{max}}(\mathbf{r})}{\mathcal{J}_{\text{in}}} \leq \mathcal{O}^2 \left[\frac{A}{\lambda_{\text{rad}} z} \right]^2 \omega_{\text{meas}}^4 \Upsilon_{\text{meas}}(\mathbf{r}) , \quad (2.41a)$$

where

$$\Upsilon_{\text{meas}}(\mathbf{r}) = \frac{\max_t \sum_{n=1}^N A_n |\partial_t^3 f_n(\mathbf{r}_n, t)|^2}{\sum_{n=1}^N A_n \int_{-\infty}^{\infty} dt |\partial_t^3 f_n(\mathbf{r}_n, t)|^2} . \quad (2.41b)$$

As in the radiated-field case, one can design the LW driving functions to obtain the measured-field relation:

$$\Upsilon_{\text{LW}}^{\text{meas}} \gg \Upsilon_{\text{CW}}^{\text{meas}} . \quad (2.42)$$

D. Discussion

One would like to anticipate the results indicated by the radiated and measured-field energy bounds. The CW case is the easiest since the radiated and measured beam values will essentially be the same. Beyond the Rayleigh distance $L_{\text{rad}}^{\text{CW}}$, the energy in the CW radiated and measured fields decays as $1/r^2$. Thus, as depicted in Fig. 3, a graph on a log-log plot of the efficiency $\Gamma_{\text{rad}}^{\text{CW}}$ of the CW beam as a function of the distance from the array results in a straight line with slope of -2 . Let us select Ω_{rad} as the CW frequency. According to (2.22), the LW beam can then be designed to be slightly more efficient than this CW case even in its radiated far-field energy. The moving interference pattern behavior of the LW beam governs its near-field properties. As mentioned above, the correlation function Λ_{mn} for the radiated or measured fields can be made to increase as the range increases. This allows the beam launched from a LW-driven array to maintain its shape as it propagates away from the array. As a result, the efficiency of this beam remains relatively unchanged in the near field. On the other hand, the quality of the near-field beam of a uniformly driven CW array is poor because large constructive and destruc-

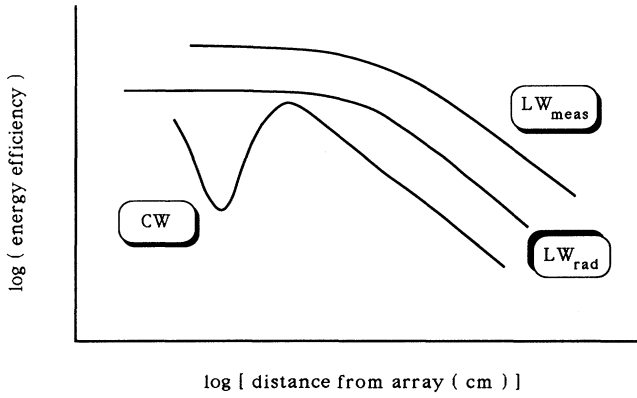


FIG. 3. Anticipated bounds on the energy-efficiency decay rates.

tive interference regions are formed. The efficiency of the CW beam will then have large peaks and valleys in its near field. Thus one expects the LW efficiency curves shown in Fig. 3. The efficiency level of the LW radiated field is slightly greater than the final peak of the CW case in the near field, and the LW beam will maintain its localization over an extended distance. This LW efficiency curve will be above the CW efficiency curve since its far-field value is greater than the CW value; it will finally exhibit a $1/r^2$ behavior when its Rayleigh distance $L_{\text{rad}}^{\text{LW}}$ is surpassed. The LW measured-field efficiency will be very similar in shape to its radiated-field counterpart, but it will exhibit the enhanced values expected from (2.30). This qualitative analysis will be supported with numerical results in Sec. III. Thus we expect that one can achieve (1) enhanced localization of the transmitted and measured beam energy; (2) higher transmitted beam intensity; and (3) higher measured beam energy.

With the bounds presented above, the diffraction lengths associated with the various quantities under discussion can be quantified more precisely. As in the radiated-beam-energy case, the bound (2.20) naturally defines the diffraction length

$$L_{\text{rad}}^{\text{energ}} = \frac{A}{\lambda_{\text{rad}}} . \quad (2.43)$$

Now consider the radiated-beam-intensity and measured-beam-energy bounds. A natural length can be extracted from the intensity bound (2.38) by multiplying it by a time characteristic of the array driving functions to yield a dimensionless fluence ratio (maximum point value over input average). For example, choosing $1/\omega_{\text{rad}}$ as the natural time associated with the pulse-driven array, one can rewrite (2.38) as

$$\frac{\mathcal{J}_{\text{rad}}^{\text{max}}(\mathbf{r})}{\omega_{\text{rad}} \mathcal{F}_{\text{in}}} \leq \left[\frac{A}{\lambda_{\text{rad}}^{\text{int}} z} \right]^2 \equiv \left[\frac{L_{\text{rad}}^{\text{int}}}{z} \right]^2 , \quad (2.44a)$$

where the diffraction length $L_{\text{rad}}^{\text{int}}$ of the radiated beam intensity

$$L_{\text{rad}}^{\text{int}} = \left[\frac{\Upsilon_{\text{rad}}}{\omega_{\text{rad}}} \right]^{1/2} L_{\text{rad}}^{\text{energ}} . \quad (2.44b)$$

Similarly, one can normalize the measured-beam-energy bound (2.30) by a term $\mathcal{E}^2 \omega_{\text{rad}}^4$ that depends on the same choice for the natural frequency associated with the array driving functions and that characterizes the energy conversion processes in the transmitter and receiver systems. This yields the expression

$$\frac{\mathcal{F}_{\text{meas}}}{(\mathcal{E}^2 \omega_{\text{rad}}^4) \mathcal{F}_{\text{in}}} \leq \left[\frac{A}{\lambda_{\text{meas}}^{\text{energ}} z} \right]^2 \equiv \left[\frac{L_{\text{meas}}^{\text{energ}}}{z} \right]^2 , \quad (2.45a)$$

where the diffraction length $L_{\text{meas}}^{\text{energ}}$ of the measured beam energy

$$L_{\text{meas}}^{\text{energ}} = \left[\frac{\omega_{\text{meas}}}{\omega_{\text{rad}}} \right]^2 L_{\text{rad}}^{\text{energ}} . \quad (2.45b)$$

Clearly, these diffraction lengths depend upon the choice of the natural frequency associated with the set of signals driving the array, as does the CW comparison beam. However, the choices are the same in both cases. If Ω_{rad} had been chosen, then, for instance, the natural diffraction length associated with the radiated beam energy would be

$$L_{\text{rad}}^{\text{energ}} = \left[\frac{\omega_{\text{rad}}}{\Omega_{\text{rad}}} \right] \mathcal{L}_{\text{rad}}^{\text{energ}} , \quad (2.46)$$

where $\mathcal{L}_{\text{rad}}^{\text{energ}} = A \Omega_{\text{rad}} / (2\pi c z)$. This yields the same conclusions described above. Thus, having made such a choice, one can associate diffraction lengths with each of the beam characteristics. An equivalent alternative is to compare the beam performances by dividing the LW value by the CW value and rearranging the terms. The resulting expressions will be dimensionless and independent of z . The diffraction lengths thus obtained are identical to those discussed above.

The rate of divergence of the beam generated by a pulse-driven array can now be obtained as well. The rate of expansion of a beam can be quantified by measuring the radius at which its fluence profile has decreased to half its maximum value in the plane $z = \text{const}$ away from the aperture. This radius value, the half width at half maximum (HWHM) of the fluence profile, is a good measure of the transverse localization of the beam. This is analogous to the definition of the waist of a CW Gaussian beam. Consider the measured-field fluence expression:

$$\mathcal{F}_{\text{meas}}(\mathbf{r}) = \mathcal{E}^2 \left[\frac{1}{2\pi c} \right]^2 \sum_{m=1}^N \sum_{n=1}^N \frac{A_m^{1/2} A_n^{1/2}}{R_m R_n} \Lambda_{mn}^{\text{meas}}(\mathbf{r}) \times \mathcal{W}_m^{1/2} \mathcal{W}_n^{1/2} , \quad (2.47)$$

which led to the bound (2.26). The terms $\Lambda_{mn}^{\text{meas}}(\mathbf{r}) / (R_m R_n)$ clearly control the observation point dependence of the beam. Since the convolutions

$$\int_{-\infty}^{\infty} dt \partial_t^3 f_m(\mathbf{r}_m, t - R_m/c) \partial_t^3 f_n(\mathbf{r}_n, t - R_n/c) = \int_{-\infty}^{\infty} d\tau \partial_t^3 f_m(\mathbf{r}_m, \tau) \partial_t^3 f_n(\mathbf{r}_n, \tau - (R_n - R_m)/c) \\ \equiv (A_m A_n \mathcal{W}_m \mathcal{W}_n)^{1/2} \Lambda_{mn}^{\text{meas}}(\mathbf{r}), \quad (2.48)$$

the beam fluence decreases as the array driving functions become uncorrelated. In the far field the distance factor $(R_m R_n)^{-1} \sim z^{-2}$ and the time factor $(R_n - R_m)/c \sim (\mathbf{r}_m - \mathbf{r}_n) \cdot \mathbf{r}/cz$. Thus the off-axis behavior rests solely with the convolution terms (2.48). Those terms decrease to half their value when their arguments experience a time shift approximately equal to a quarter of their characteristic time period. In the measured-field case this occurs when $(R_n - R_m)/c \sim T_{\text{meas}}/4 = (\pi/2\omega_{\text{meas}})$. Accounting for the variations in the driving time signals across a planar array, the HWHM of the far-field measured energy profile occurs at the radius

$$\rho_{\text{meas}}^{\text{HWHM}} \approx \left(\frac{\lambda_{\text{meas}}}{4d_{\text{max}}} \right) z, \quad (2.49a)$$

where d_{max} is the largest distance between the significant time signals in the array, usually the maximum radius of an element in the array. The rate of the divergence of the beam is simply $\theta_{\text{meas}} = \rho_{\text{meas}}^{\text{HWHM}}/z \sim \lambda_{\text{meas}}/(4d_{\text{max}})$. The corresponding radiated-field value is

$$\rho_{\text{rad}}^{\text{HWHM}} \approx \left(\frac{\lambda_{\text{rad}}}{4d_{\text{max}}} \right) z. \quad (2.49b)$$

The beam generated by a CW pulse-driven array of diameter $D = 2d_{\text{max}}$ will then diverge at the rate $\theta_{\text{rad}} \equiv \theta_{\text{meas}} \approx \frac{1}{2} \lambda_{\text{CW}}/D$. Because one can control *by design* the correlation properties of the constituent time signals as well as satisfaction of the effective frequency condition (2.33b) (i.e., the relative arrival times and the amounts of the various frequency components), the beam generated by a LW pulse-driven array can be made more localized than the corresponding CW beam:

$$\frac{\theta_{\text{meas}}^{\text{LW}}}{\theta_{\text{meas}}^{\text{CW}}} = \frac{\omega_{\text{meas}}^{\text{CW}}}{\omega_{\text{meas}}^{\text{LW}}} \ll 1. \quad (2.50)$$

Note that even if there were not a gain in efficiency in the LW case, the increase in the distance over which localization can be maintained may be more significant. Any performance comparison clearly depends on the intended application of the beam. If one is interested in secure communications, for example, the maintenance of beam quality with low sidelobe levels is of the utmost importance. If one is simply interested in weapons applications, then one would expect that the more efficiency one has, the better. This is not true if the trade-off for large efficiencies is large sidelobe levels. Fratricide issues can become extremely important. In particular, why not attempt to drive the array with a CW frequency corresponding to the absolute bandwidth? The bound (2.20) would suggest such a choice if the largest radiated-field efficiency is desired. One finds that for a given set of radi-

ating elements, going to higher-frequency values in the CW case maintains the on-axis efficiency at the cost of very large sidelobes, the so-called grating lobes. These grating lobes appear when the wavelength of the CW signal becomes smaller than the element spacing. They do not appear when the proper broad-bandwidth driving functions are used. For communication and remote sensing applications, this cost of maintaining the beam's brightness may be too high. As shown in Ref. [14] and below, a broad-bandwidth signal set can be designed to drive an array and produce a beam with high efficiency and very low sidelobe levels. Another possibility would be to drive each element in an array with the same broad-bandwidth signal $f_0(t)$. If the resulting input energy is identical to the LW case: $A \int_{-\infty}^{\infty} |f_0|^2 dt = \sum_{n=1}^N A_n \int_{-\infty}^{\infty} |f_n|^2 dt$, the corresponding frequency spectrum $F_0(\omega)$ satisfies the relation $\omega^{2j} |F_0(\omega)|^2 = \sum_{n=1}^N (A_n/A) \omega^{2j} |F_n(\omega)|^2$ for any integer j . Thus the effective frequency ω_{meas} , hence the diffraction length associated with the measured energy of the beam, would be the same in both cases. Although this approach seems straightforward, it has two drawbacks. The first is the loss in localization that occurs when the spatial degree of freedom is not utilized. To achieve the entire spectrum associated with the set of LW driving functions, the time signal $f_0(t)$ must necessarily be longer in time than any of those LW signals. Thus the convolutions will persist for a longer time giving a larger transverse distance, hence, faster rate of divergence than with the LW beam. This faster rate of divergence for a beam generated by an array driven with a single broad-bandwidth time signal having the same frequency content as the LW case has been confirmed experimentally. The second drawback is one of practicality. The requisite signal $f_0(t)$ will be much more complicated than any of the individual LW driving signals; and hence, more complex wave form generators and radiators would be required to produce it. This increase in complexity combined with the decrease in localization would severely limit the usefulness of such an input field scheme.

Note also that if the fields from each radiating element are measured independently in the far field of the array at a distance z_1 along the array axis and are then combined, a bound on the fluence of the total field measured at a more distant point z_2 is given by

$$\mathcal{F}_{\text{meas}}(z_2) \leq \left(\frac{z_1}{z_2} \right)^2 \mathcal{F}_{\text{meas}}(z_1) \quad (2.51a)$$

or

$$\frac{\mathcal{F}_{\text{meas}}(z_2)}{\mathcal{F}_{\text{meas}}(z_1)} \leq \left(\frac{z_1}{z_2} \right)^2. \quad (2.51b)$$

This is also true of the radiated-field fluences as well. This result follows immediately from (2.20) and (2.30) and was proved independently in Ref. [12]. Unfortunately, this result does not give a comparison of a LW pulse-driven array to the CW-driven equivalent, nor does it indicate how far the localization region extends. It must be satisfied in the far field by any finite-energy beam. As suggested by Ref. [12], the quantity on the left-hand side of (2.34b) could be considered as an efficiency. This would be a bound on the measured-field energy versus the field energy measured at some point or set of points closer to the array. Since this result makes no connection with the energy of the input driving functions, it says nothing about the overall efficiency of the radiating system. It makes no direct connection with the energy contained in the various spectral components actually driving the array elements and the measured-field energies. The expressions for the radiated- and measured-field fluences normalized by the input fluence fairly represent the efficiencies of a pulse-driven array.

III. NUMERICAL RESULTS

We will assume below a perfect array (one with no restrictions on bandwidth or rise times, etc.) for comparison purposes. The array will thus be the same for any set of input driving functions. Given such an array, one has only the freedom of choosing the input signals. Avoiding the singular (infinite derivative) cases discussed in Sec. II A, we will compare below the radiated- and the measured-field intensities and energy efficiencies of beams generated by various LW pulse-driven arrays and the corresponding CW cases based only upon the radiated-field effective frequency criteria involving Ω_{rad} and ω_{rad} . Additional possible enhancements in these performance criteria would be expected for a spectral point criterion such as the 3-dB frequency value; these improvements will also be noted during the discussion.

Note that a CW signal theoretically has an infinite duration and is thus not physically realizable. It has been shown [14] that an array driven with a time-windowed CW signal (a CW tone burst) is slightly less efficient than one driven with a pure, infinite-duration CW signal because more energy will leak into its sidelobes. The bounds derived in Sec. II are thus the most stringent possible. The numerical comparisons made below will deal with finite-duration CW tone bursts. Since the tone burst needs about four or five cycles to establish its CW nature, each CW case will deal with several periods.

To begin the discussion, the various types of array excitation schemes will be pointed out. Note that the Huygens representation of the field (2.2) can be written in its most general form as [21]

$$g(\mathbf{r}, t) = \int_S \beta,$$

where β is the closed 2-form $\Psi dS / (4\pi R)$ and S is the plane $z = \text{const}$. If A represents the surface of the array, this can be rewritten simply as

$$g(\mathbf{r}, t) = \int_A \beta + \int_{S-A} \beta.$$

The Huygens-Kirchhoff representation gives

$$g(\mathbf{r}, t) \approx \int_A \beta,$$

neglecting the contributions from the complement of A in S , as noted in Sec. II. If a LW solution is used to drive the array in the straightforward scheme, only the portion of that solution that has its support over A will contribute to the resulting beam. This scheme truncates the exact solution and one expects, more or less, the standard diffraction effects. On the other hand, if the array were of infinite extent, then the input field is recovered away from the array, i.e., $g \equiv f$; and the beam generated from the array reproduces the localized effects of the exact solution. A finite array driven with the modified-power-spectrum (MPS) pulse will be considered below.

Since the array is assumed to be finite, one could try to take a portion of the complement of A and introduce the information contained in the second integral over that subset back into the array. One such attempt, the folded array introduced in Ref. [3], uses a conformal map μ that takes a subset Σ of A into a portion B of $S - A$; i.e., the push forward $\mu_* \Sigma = B$ so that if μ^* is the associated pull back, then one has the field

$$g(\mathbf{r}, t) \approx \int_A \beta + \int_B \beta = \int_A \beta + \int_\Sigma (\mu^* \beta).$$

This procedure has increased the complexity of the driving signals distributed over the array. From the bounds derived above, we now know that at most this mapping can increase significantly the radiated or measured effective frequencies; and we can at most expect it to give some enhanced diffraction length. It cannot create a diffraction-free beam since even the exact, finite-energy LW solution eventually succumbs to diffraction effects. The behavior of the beams created by this folded array will be described below.

Many other schemes are possible. For instance, since the 2-form β is closed, Poincaré's theorem [21] tells us that there exists a 1-form α such that $d\alpha = \beta$ over $S - A$. If $C = \partial(S - A)$ is the boundary of the surface $S - A$, one can then write

$$g(\mathbf{r}, t) = \int_A \beta + \int_{S-A} \beta = \int_A \beta + \int_C \alpha.$$

Note that the contour $C = -\partial A$. This result is related to the Maggi-Rubinowicz representation [22,23] where one tries to represent the field generated by the aperture A in terms of a boundary diffraction wave originating from ∂A . Here, we are including an additional term to complement the original aperture distribution. However, the bounds again indicate that this procedure can at most enhance the localization properties of the beam over some specified, finite distance if it has finite energy.

A. Simple MPS pulse-driven array

Consider the case of a circular aperture of radius R_a driven with signals defined by the MPS pulse [3]:

$$f(\mathbf{r}, t) = \text{Re} \frac{1}{z_0 + i(z - ct)} \frac{1}{[(s/\beta) + a]^\alpha} e^{-bs/\beta}, \quad (3.1)$$

where $s(\rho, z, t) = \rho^2 / [z_0 + i(z - ct)] - i(z + ct)$ and the transverse distance $\rho = (x^2 + y^2)^{1/2}$. The operator Re takes the real part of the entire expression to its right. The parameters that will be used here and that have been used for all of the ultrasound experiments in water are $a = 1.0$ m, $\alpha = 1.0$, $b = 6.0 \times 10^2$ m⁻¹, $\beta = 3.0 \times 10^2$, and $z_0 = 4.5 \times 10^{-4}$ m. The speed of sound in water $c = 1.50 \times 10^3$ m/s. This solution has the transverse waist $w = (\beta z_0 / b)^{1/2}$ at $z = t = 0$ and the maximum frequency $f_{\text{max}} = c / (2\pi z_0) = c / \lambda_{\text{min}}$ that represents here the 1/e folding point of the amplitude of its Fourier spectrum.

As shown in Appendix B, the distance over which the MPS beam maintains its amplitude, essentially the diffraction length of the radiated-field intensity, is given by the expression

$$L_{\text{MPS}} \approx \frac{\pi w R_a}{\lambda_{\text{min}}} . \quad (3.2)$$

To use this formula it is assumed that $w \leq R_a$; otherwise, if the waist $w > R_a$, then the waist w is simply set to the value R_a . On the other hand, if this aperture is driven with a CW Gaussian beam having the frequency f_{max} with the same waist w , the diffraction length of the resulting beam is

$$L_G = \frac{\pi w^2}{\lambda_{\text{min}}} . \quad (3.3)$$

Similarly, if the entire aperture is driven uniformly with a CW signal having the frequency f_{max} , then the diffraction length of the resulting beam is

$$L_R = \frac{\pi R_a^2}{\lambda_{\text{min}}} . \quad (3.4)$$

As shown in Appendix C, this result holds even when the driving signal is a CW tone burst. Since $w \leq R_a$, one has explicitly

$$L_G \leq \left[\frac{R_a}{w} \right] L_G \equiv L_{\text{MPS}} \equiv \left[\frac{w}{R_a} \right] L_R \leq L_R . \quad (3.5)$$

Therefore, as claimed in Refs. [3] and [9], the MPS pulse-driven aperture can be made to have a longer diffraction length than the corresponding CW Gaussian pulse-driven array simply by choosing $w < R_a$.

Although (3.5) explicitly compares the radiated-field-intensity diffraction lengths, it says nothing about the overall quality of the corresponding aperture-generated beams. In the near field, one finds that the pencil-like beam quality of the MPS pulse-driven aperture-generated field is similar to the Gaussian case. In contrast, the near field of the piston case consists of many large regions exhibiting the effects of constructive and destructive interference and thus an extremely poor beam quality there, even though its intensity can be maintained further, far beyond its diffraction length, the MPS beam splits and forms off-axis lobes giving a $1/z^2$ decay along the axis of the aperture. The beams for both the Gaussian and piston cases exhibit the usual $1/z$ decay along that axis. The half width (radius) of the beam at half the

maximum of its intensity profile takes the value

$$w_G(z) \sim w \left[\frac{z}{L_G} \right] = \left[\frac{\lambda_{\text{min}}}{\pi w} \right] z . \quad (3.6)$$

As noted above, this "half-width at half-maximum" value is usually called the waist of the beam. Similarly, the piston beam waist is given approximately by the expression

$$w_P(z) \sim \left[\frac{\lambda_{\text{min}}}{4R_a} \right] z . \quad (3.7)$$

Note that for the Gaussian case one has $w \leq R_a$. Thus the beam generated in the piston case is narrower than the one obtained in the Gaussian case. This behavior is related to the natural focusing of the piston beam that occurs in the near-field region of the array.

Now consider the energy bounds and beam-divergence rates discussed in Sec. II. The far-field radiated- and measured-field effective frequencies can be obtained analytically for the MPS pulse (3.1) through their frequency-domain expressions:

$$\omega_{\text{rad}}^2 = \frac{\int_0^{R_a} d\rho \rho \int_{-\infty}^{\infty} d\omega \omega^2 |F(\rho, z=0, \omega)|^2}{\int_0^{R_a} d\rho \rho \int_{-\infty}^{\infty} d\omega |F(\rho, z=0, \omega)|^2} , \quad (3.8)$$

$$\omega_{\text{meas}}^4 = \frac{\int_0^{R_a} d\rho \rho \int_{-\infty}^{\infty} d\omega \omega^6 |F(\rho, z=0, \omega)|^2}{\int_0^{R_a} d\rho \rho \int_{-\infty}^{\infty} d\omega \omega^2 |F(\rho, z=0, \omega)|^2} ,$$

where $F(\rho, z=0, \omega)$ is the Fourier transform of the MPS pulse (3.1) in the plane of the aperture:

$$F(\rho, z=0, \omega) = \int_{-\infty}^{\infty} dt e^{-i\omega t} f(\rho, z=0, t) . \quad (3.9)$$

When $\rho=0$, one has exactly

$$\begin{aligned} F(\rho=0, z=0, \omega) &= \frac{1}{z_0 a} \frac{2\pi z_0}{c} \frac{\beta a}{\beta a - z_0} H \left[\frac{\omega}{c} - \frac{b}{\beta} \right] \\ &\quad \times (e^{-z_0(\omega/c - b/\beta)} - e^{-\beta a(\omega/c - b/\beta)}) \\ &\sim \frac{1}{z_0 a} \frac{2\pi z_0}{c} H \left[\frac{\omega}{c} - \frac{b}{\beta} \right] e^{-z_0(\omega/c - b/\beta)} , \end{aligned} \quad (3.10a)$$

where $H(x)$ is the Heaviside function. The second form is an extremely good approximation because $\beta a \gg 1$. Similarly, off axis one has

$$\begin{aligned} F(\rho, z=0, \omega) &\sim \frac{1}{z_0 a} \frac{2\pi z_0}{c} H \left[\frac{\omega}{c} - \frac{b}{\beta} \right] e^{-z_0(\omega/c - b/\beta)} \\ &\quad \times J_0 \left[2\rho \left[\frac{b}{\beta} \left[\frac{\omega}{c} - \frac{b}{\beta} \right] \right]^{1/2} \right] . \end{aligned} \quad (3.10b)$$

The terms associated with the second exponential factor appearing in (3.10a) when $\rho \neq 0$ are likewise exponentially smaller than those retained in this expression. Note that the second exponential term governs the behavior of the spectrum when $\omega \sim bc/\beta$. The exact spectrum does not

have a discontinuity there, as one might infer from the approximate forms (3.10a) and (3.10b). These forms suggest the introduction of the minimum and maximum frequency parameters: $\omega_{\min} = bc/\beta$ and $\omega_{\max} = c/z_0$. The Fourier transform (3.10) can then be written in the physically appealing form

$$F(\rho, z=0, \omega) \sim \frac{1}{z_0 a} \frac{2\pi}{\omega_{\max}} H(\omega - \omega_{\min}) e^{-(\omega - \omega_{\min})/\omega_{\max}} \times J_0(2(\rho/c)[\omega_{\min}(\omega - \omega_{\min})]^{1/2}). \quad (3.11)$$

Let us introduce the terms

$$W_n(p) = \left[\frac{1}{2p^2} \right]^{n+1} \left[\left[\xi^2 \frac{d}{d\xi} \right]^n \mathcal{W}(\xi) \right]_{\xi=p^2}, \quad (3.12a)$$

$$\mathcal{W}(\xi) = \xi^2 e^{-\xi} [I_0(\xi) + I_1(\xi)], \quad (3.12b)$$

where $I_n(x)$ is the modified Bessel function of the first kind of order n . Inserting (3.10) into (3.8) and performing the ρ integration, one obtains, for instance, that

$$\begin{aligned} \omega_{\text{rad}}^2 &= \omega_{\text{max}}^2 \frac{\int_0^\infty dx (x + \omega_{\min}/\omega_{\max})^2 e^{-2x} [J_0^2(2(R_a/w)\sqrt{x}) + J_1^2(2(R_a/w)\sqrt{x})]}{\int_0^\infty dx e^{-2x} [J_0^2(2(R_a/w)\sqrt{x}) + J_1^2(2(R_a/w)\sqrt{x})]} \\ &= \omega_{\text{max}}^2 \frac{W_2(R_a/w) + 2(\omega_{\min}/\omega_{\max})W_1(R_a/w) + (\omega_{\min}/\omega_{\max})^2 W_0(R_a/w)}{W_0(R_a/w)} \\ &\sim \omega_{\text{max}}^2 \frac{W_2(R_a/w)}{W_0(R_a/w)}, \end{aligned} \quad (3.13)$$

since $\omega_{\min}/\omega_{\max} \ll 1$ for the broad-bandwidth pulse under consideration. Similarly, one can also show that

$$\omega_{\text{meas}}^4 \sim \omega_{\text{max}}^4 \frac{W_6(R_a/w)}{W_2(R_a/w)}. \quad (3.14)$$

Note that these results are all in terms of the ratio of the radius of the aperture to the initial waist of the MPS pulse: R_a/w . Since to a reasonable approximation, $I_0(x) \sim e^x(1+1/8x)/\sqrt{2\pi x}$ and $I_1(x) \sim e^x(1-3/8x)/\sqrt{2\pi x}$ for $x > 1$, after some tedious and lengthy algebra one obtains, with $p = R_a/w > 1$,

$$W_0(p) = \frac{e^{-p^2}}{2} [I_0(p^2) + I_1(p^2)] \sim \frac{1}{\sqrt{2\pi p}} [1 + O(p^{-2})], \quad (3.15a)$$

$$W_2(p) = \frac{e^{-p^2}}{8} [(2-p^2)I_0(p^2) + p^2 I_1(p^2)] \sim \frac{1}{\sqrt{2\pi p}} \left[\frac{3}{16} + O(p^{-2}) \right], \quad (3.15b)$$

$$\begin{aligned} W_6(p) &= \frac{e^{-p^2}}{128} [(-16p^{10} + 228p^8 - 1095p^6 + 2178p^4 - 1800p^2 + 720)I_0(p^2) \\ &\quad + (16p^{10} - 220p^8 + 987p^6 - 1710p^4 + 1044p^2)I_1(p^2)] \\ &\sim \frac{1}{\sqrt{2\pi p}} \left[\frac{3}{128} p^6 + O(p^4) \right]. \end{aligned} \quad (3.15c)$$

Therefore the effective frequencies of the MPS radiated and measured fields are

$$\omega_{\text{rad}}^2 \sim \frac{3}{16} \omega_{\text{max}}^2, \quad (3.16a)$$

$$\omega_{\text{meas}}^4 \sim \frac{1}{8} \left[\frac{R_a}{w} \right]^6 \omega_{\text{max}}^4 = \left[\frac{R_a^2}{2w^2} \right]^3 \omega_{\text{max}}^4. \quad (3.16b)$$

Using the expressions for the wavelengths associated with the diffraction lengths for the radiated- and measured-field energies derived in Sec. II, one can now obtain those lengths for the present case:

$$L_{\text{rad}}^{\text{MPS}} = \frac{\pi R_a^2}{\lambda_{\text{rad}}^{\text{energ}}} \sim \sqrt{3/16} L_R = \sqrt{3/16} \left[\frac{R_a}{w} \right]^2 L_G, \quad (3.17a)$$

$$L_{\text{meas}}^{\text{MPS}} = \left[\frac{\omega_{\text{meas}}}{\omega_{\text{rad}}} \right]^2 L_{\text{rad}}^{\text{MPS}}$$

$$= \frac{16}{3} \left[\frac{R_a^2}{2w^2} \right]^{3/2} L_{\text{rad}}^{\text{MPS}}$$

$$= \sqrt{16/3} \left[\frac{R_a^2}{2w^2} \right]^{3/2} L_R = \sqrt{2/3} \left[\frac{R_a}{w} \right]^5 L_G. \quad (3.17b)$$

These results indicate that when the MPS parameters are chosen so that $w < R_a$, the diffraction length associated

with the radiated-field energy of the MPS pulse-driven array can be made larger than its value in the corresponding Gaussian case, and that the diffraction lengths associated with the measured-field energy can be made larger than its value in the corresponding piston, and hence Gaussian, cases. Similarly the waists of the radiated and measured beams are

$$\begin{aligned} w_{\text{MPS}}^{\text{rad}}(z) &\sim \frac{\lambda_{\text{rad}}}{4R_a} \\ &= \frac{4}{\sqrt{3}} \left[\frac{\lambda_{\text{min}}}{4R_a} \right] = \frac{4}{\sqrt{3}} w_p(z) = 1.81 \left[\frac{w}{R_a} \right] w_G(z), \end{aligned} \quad (3.18a)$$

$$\begin{aligned} w_{\text{MPS}}^{\text{meas}}(z) &\sim \frac{\lambda_{\text{meas}}}{4R_a} \\ &= \left[\frac{2w^2}{R_a^2} \right]^{3/4} \frac{\lambda_{\text{min}}}{4R_a} = \left[\frac{2w^2}{R_a^2} \right]^{3/4} w_p(z) \\ &= 1.32 \left[\frac{w}{R_a} \right]^{5/2} w_G(z). \end{aligned} \quad (3.18b)$$

These results indicate that when the MPS parameters are chosen so that $w < R_a$, the waist of the beam generated by the MPS pulse-driven array can be made smaller than its value in the corresponding Gaussian case, and that the waist of the beam associated with the LW measured-field energy can be made smaller than its value in the corresponding piston, and hence Gaussian, cases.

It is noted that the piston case corresponds naturally to a focused aperture. Focusing to a spot whose radius is smaller than R_a can occur only within the near field of an aperture and only occurs in one $z = \text{const}$ plane in that near field. Away from the focal plane the beam quality is poor until the far field is reached. For the piston case the natural focus occurs at $R_a^2/\lambda_{\text{min}}$ and the far field is reached at L_R (see Appendix C). Since the Gaussian case results in a beam whose quality is maintained from the aperture to the observation point, it is the one usually chosen for many applications such as remote sensing and communications, even though it has a shorter diffraction length. Moreover, because the beam localization is more important than the maximum intensity or energy efficiency for those applications, the aperture is driven with a Gaussian whose waist $w < R_a$. The MPS pulse-driven aperture is then an improvement over that Gaussian case in both the beam localization, maximum intensity, and energy efficiency of the radiated and measured fields. This has been confirmed experimentally [9,10].

In the MPS pulse-driven-array experiments described in Refs. [9] and [10], the radius of the array $R_a = 3.0$ cm,

giving the ratio $R_a/w = 2$; and the maximum frequency $f_{\text{max}} = 0.53$ MHz, giving $L_G = 24.98$ cm and $L_R = 99.90$ cm. The array was square and consisted of 21×21 elements, uniformly spaced with 0.3 cm between elements. For comparison purposes, the experiment was designed to compare the MPS pulse-driven-array results to the CW Gaussian and piston cases with the frequency $f = 0.5$ MHz $\sim f_{\text{max}}$. A circular array was effected by zeroing the amplitudes of the signals on the elements whose radii exceeded R_a . Because $\omega_{\text{meas}} = 1.68\omega_{\text{CW}}$, the (theoretical) measured-field-energy diffraction length (3.17b) is $L_{\text{meas}}^{\text{MPS}} = (\omega_{\text{meas}}/\omega_{\text{CW}})^2 L_{\text{meas}}^{\text{CW,P}} = (R_a^2/2w)^{3/2} L_{\text{meas}}^{\text{CW,P}} = 2.83 L_{\text{meas}}^{\text{CW,P}} = 11.31 L_{\text{meas}}^{\text{CW,G}}$. Experimentally, it was shown that the MPS measured-field-energy diffraction length was slightly greater than 150 cm $\sim 1.5 L_{\text{meas}}^{\text{CW,P}} \sim 6.0 L_{\text{meas}}^{\text{CW,G}}$, where $L_{\text{meas}}^{\text{CW,P}}$ and $L_{\text{meas}}^{\text{CW,G}}$ are, respectively, the calculated diffraction lengths for the 0.5-MHz CW piston and Gaussian amplitude weighted cases. The (theoretical) waist (3.18b) of the measured beam energy is $w_{\text{meas}}^{\text{MPS}}(z) = 0.59 w_p(z) = 0.23 w_G(z)$ which gives 4.29 as the ratio of the beam expansion rates for the 0.5-MHz CW Gaussian and MPS cases. Experimentally, this ratio was found approximately to be 6.75. It is believed that the discrepancies between the experimental and theoretical diffraction length and beam-divergence results are due to a number of factors, mostly experimental in nature. A small amount of error is introduced by the approximations leading to the values given by (3.16) and by the difference between the discrete experimental array and the continuous aperture distribution used to derive the theoretical values. Round-off errors in the driving signals were generated by the original set of electronics used in the one- and two-dimensional synthetic array experiments under consideration here. Those round-off errors tended to smooth the output signals, generally producing a lower-than-expected measured effective frequency for the LW case. The worst experimental beams were consistently produced by the 0.5-MHz CW case making the above quantitative comparisons difficult. For instance, the experimental diffraction length of the 0.5-MHz CW beam appeared to be less than the first possible measurement point at 25.0 cm. Better quality beams were produced when the array was driven with 1.0 and 2.0-MHz CW signals, making the comparisons more definite. For example, the MPS beam waist was found to be $\sim 95.0\%$ of the waist of the beam generated by driving the array with a 2.0-MHz CW Gaussian. This means $w_{\text{meas}}^{\text{MPS}} \sim (0.95)0.25 w_G(z) = 0.24 w_G(z)$, in excellent agreement with the theoretical value. Even with some discrepancies between the theoretical and experimental results, these early experiments support the theoretical view that narrower, more efficient beams are possible using LW pulse-driven arrays.

B. Folded MPS pulse-driven array

Consider now the folded array introduced in Ref. [3]. As discussed above, the folded array represents an attempt to include more information about the exact LW

solution into the array driving signals. The conformal mapping used here is simply $\rho \rightarrow R_{\max}^2/\rho$, which maps an annulus with its radii greater than the maximum array radius R_{\max} into an annulus with its radii smaller than R_{\max} .

Because the calculations are not readily tractable

$$S(\rho, t) = \begin{cases} w(t)f(\rho, z=0, t) & (\rho=0) \\ w(t)[f(\rho, z=0, t) + (R_{\max}/\rho)^4 f(R_{\max}^2/\rho, z=0, t-t_d)] & (\rho \neq 0) \end{cases}, \quad (3.19)$$

where $R_{\max} = (x_{\max}^2 + y_{\max}^2)^{1/2}$ is the maximum radius of the source locations in the array and the position-dependent delay time $t_d = \{[z_d^2 + (R_{\max}^2/\rho)^2]^{1/2} - [z_d^2 + \rho^2]^{1/2}\}/c$, the constant-delay distance being $z_d = 3.0 \times 10^{-2}$ m. If $h(t, \tau) = 0.42 - 0.50 \cos[2.0\pi(t/\tau)] + 0.08 \cos[4.0\pi(t/\tau)]$, the extra window function $w(t) = 0$ for $t < -t_1$ and for $t > t_4$; $w(t) = h(t, t_1)$ for $-t_1 < t < -t_2$ and $w(t) = h(t, t_4)$ for $+t_3 < t < +t_4$; and $w(t) = 1.0$ for $-t_2 \leq t \leq t_3$, where $t_1 = 6.0 \times 10^{-6}$ s, $t_2 = 3.0 \times 10^{-6}$ s, $t_3 = 0.5 \times 10^{-6}$ s, and $t_4 = 1.0 \times 10^{-6}$ s. The time window $w(t)$ is included in the driving signals to remove the precursor wings characteristic of the regular MPS driven arrays, hence, to minimize specifically the amount of wasted energy in those wings. The pulses (3.19) were optimized by varying the constants in (3.19) and testing them in a numerical simulation based upon (2.2)–(2.4). The desired performance, a more than ten-fold enhancement of the measured energy diffraction length, was obtained experimentally with an ultrasound array in water that was driven with these signals [10].

In order to relate the theoretical results to the experiments in Ref. [10], consider a 25-element (5×5) square array. The elements in the array are separated by 2.5 mm and are centered in 6.27×10^{-2} -cm² areas. The total length of the array on a side is thus 1.25 cm and the total area is $A = 1.5625$ cm². The actual array that was fabricated for the experiment was 1.05 cm on a side and had 0.5-mm-diameter disk elements (acoustic transducers) spaced on 2.5-mm centers. The small number of radiating elements limits the number of CW configurations; there are too few elements for any effective shading or focusing.

The LW folded array is driven with six unique signals defined by (3.19). Because of the Jacobian weighting term $(R_{\max}/\rho)^4$, the folded driving signal nearest the center of the array will have the largest amplitude. The largest distance d_{\max} between the sources of these folded signals is obtained not by comparing the actual values of their radii ρ_j , but by comparing their folded values R_{\max}^2/ρ_j . One finds $d_{\max} = 1.29$ cm. The effective frequency of the radiated far field is $f_{\text{rad}} = 0.33$ MHz. This value was obtained numerically with the signal processing code SIG [24]. This effective frequency value gives the radiated-field-energy diffraction length $L_{\text{rad}}^{\text{energ}} = L_R = 3.44$ cm. Similarly, the effective frequency associated with the measured far field is $f_{\text{meas}} = 1.435$ MHz. This effective

through analysis in this folded-array case, numerical simulations will be used to illustrate the major points. The actual driving signals were chosen from a modified version of the folded-array scheme proposed in Ref. [3] and the MPS pulse (3.1). Explicitly, a radiating element at (x, y) in the array is driven with the signal

frequency value gives the measured-field-energy diffraction length $L_{\text{meas}}^{\text{energ}} = (f_{\text{meas}}/f_{\text{rad}})^2 L_{\text{rad}}^{\text{energ}} = 18.91 L_R = 65.05$ cm. The beam divergence rate is $\theta_{\text{meas}}^{\text{LW}} = \lambda_{\text{meas}}/4d_{\max} = 2.02 \times 10^{-2}$.

The near-field effective frequency was calculated over the near-field plane $z = 1.0$ cm to be 0.173 MHz giving $\omega_{\text{rad}}/\Omega_{\text{rad}} = 1.91$. In terms of point quantities for the effective frequency, it was found that 50%, 63%, 87%, and 95% of the input energy was respectively below 0.092, 0.135, 0.33, and 0.50 MHz. Thus the $1/e^2$ frequency point coincides with the radiated energy effective frequency. The 3-dB point value for the effective frequency is $\omega_{3\text{dB}} = 0.092$ MHz giving $\omega_{\text{rad}}/\omega_{3\text{dB}} = 3.59$. Recall that these alternate values for the effective frequency all give the indicated enhancements of the radiated-field-energy diffraction length.

For theoretical comparisons, the array was driven uniformly with a CW tone burst at the frequency $f_{\text{CW}} \equiv f_{\text{rad}} = 0.33$ MHz. The tone burst is explicitly defined by the signal $f_{\text{CW}}(t) = w(t) \sin \omega_{\text{CW}} t$, where the window function $w(t) = h(|t|, \tau)$, $\tau = 12.12$ μ s. Thus there are approximately six full cycles in the tone burst. The improvements with the LW drive over the CW drive are then predicted as $(f_{\text{meas}}/f_{\text{rad}})^4$, a 345-fold enhancement in the measured-field-energy efficiency, and $\theta_{\text{meas}}^{\text{CW}}/\theta_{\text{meas}}^{\text{LW}} = (\lambda_{\text{rad}}/4R_{\max})/\theta_{\text{meas}}^{\text{LW}} = 1.607 \times 10^{-1}/2.021 \times 10^{-2}$, a decrease by a factor of 7.95 in the beam-divergence rate. For comparison purposes in the experiment, the reference CW case, in which the array was driven uniformly with a tone burst at the frequency 0.50 MHz $= 1.52 f_{\text{rad}}$, was used. Comparing the measured-field energies and divergence rates in the LW and experimental CW cases, one theoretically expects the energy to increase as $(A_{\text{expt}}/A_{\text{theor}})^2 (\omega_{\text{rad}}/\omega_{\text{CW}})^2 (f_{\text{meas}}/f_{\text{CW}})^4$, an enhancement by a factor of 12.11 in the energy, while the divergence decreases as $(\lambda_{\text{rad}}/\lambda_{\text{CW}}) \times 7.95$, a decrease by a factor of 5.21 in the divergence rate.

The numerical simulation used here to test these LW pulse-driven-array enhancements was a direct time domain implementation of (2.2c) and (2.4a). Note that the LW efficiencies will be scaled by a factor of 2 to compensate for the bipolar nature of the CW signals (the actual input energy in the CW case is twice the energy in a half period, hence, twice its average value). They will also be scaled by the square of the ratio of the near- and far-field effective frequencies $(\omega_{\text{rad}}/\Omega_{\text{rad}})^2$ given above, to

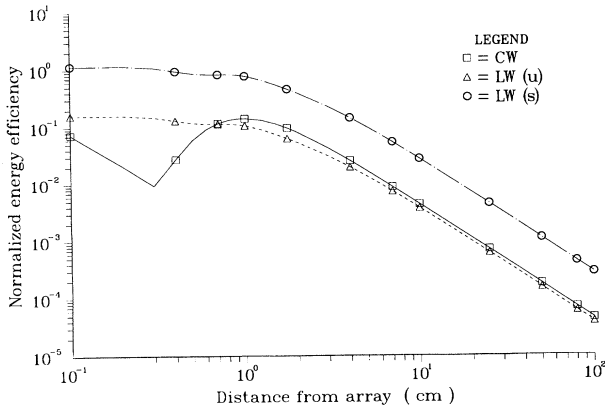


FIG. 4. Comparison of the decay of the radiated-field energy along the line-of-sight direction of the beams generated by the LW and CW pulse-driven arrays.

account for the difference between the energy launched into the medium versus the energy reaching the far field. Both unscaled and scaled results will be given.

The results are shown in Figs. 4–8. The radiated-field-energy efficiencies, the normalized radiated-field intensities, and the measured-field-energy efficiencies for the LW and CW pulse-driven arrays are compared, respectively, in Figs. 4, 5, and 7. There are 33 data points on each curve, every third one being labeled by the symbols listed in the legends. The comparisons of these actual results to those anticipated in Fig. 3 are quite good. From Fig. 4 one can see that the CW radiated-beam-energy efficiency bounds the unscaled LW folded-array case values and that the scaled LW values bound the CW results as predicted. The scaled LW to CW enhancement is 6.25. From Fig. 5 one can see that the normalized radiated-field intensities for the unscaled *and* scaled LW folded array are greater than the corresponding CW values. All of those curves have been normalized to the maximum CW value, which occurs at 0.9 cm. In the far field the LW beam intensities show, respectively, factors

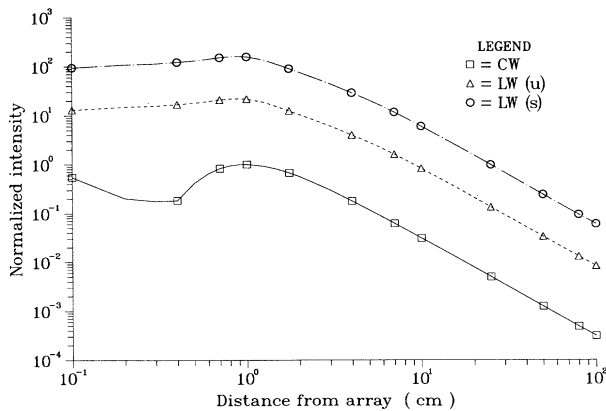


FIG. 5. Comparison of the decay of the maximum radiated-field intensities along the line-of-sight direction of the beams generated by the LW and CW pulse-driven arrays.

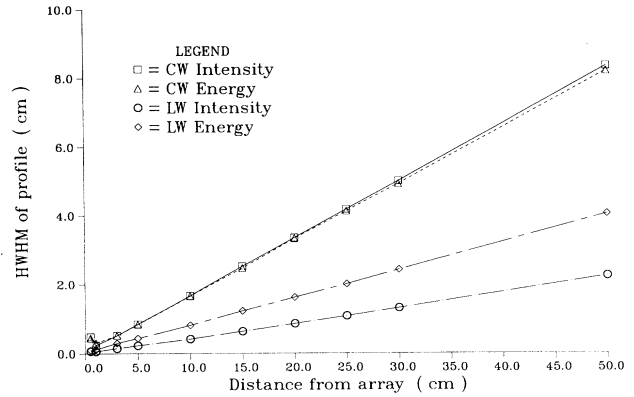


FIG. 6. Comparison of the expansion (half width at half maximum) along the line-of-sight direction of the radiated-field-energy and maximum intensity profiles of the beams generated by the LW and CW pulse-driven arrays.

of 26.60 and 193.57 improvement over the CW beam values. Similarly, from Fig. 7 one can see that the unscaled and scaled LW folded-array measured-field-energy efficiencies are much greater than the corresponding CW values. The far-field $1/z^2$ decay rate begins between 50 and 60 cm, roughly $17L_R$, which is in reasonable agreement with the predicted value. In the far field the LW beam efficiencies show, respectively, factors of 307.3 and 2236 improvement over the CW beam. The 307.3 value compares quite favorably with the predicted 345-fold improvement. In Figs. 6 and 8 the waists (HWHM) of the various beam profiles are given along the line-of-sight direction. The radiated-field beam quantities are given in Fig. 6 and the measured-field beam quantities in Fig. 8. Figure 6 shows that the LW radiated-beam-intensity and energy profiles are narrower than the corresponding CW beam profiles. The slopes of the CW beam energy and intensity profiles are 0.164 and 0.167, the corresponding LW slopes are 0.081 and 0.046. Thus the CW profiles are

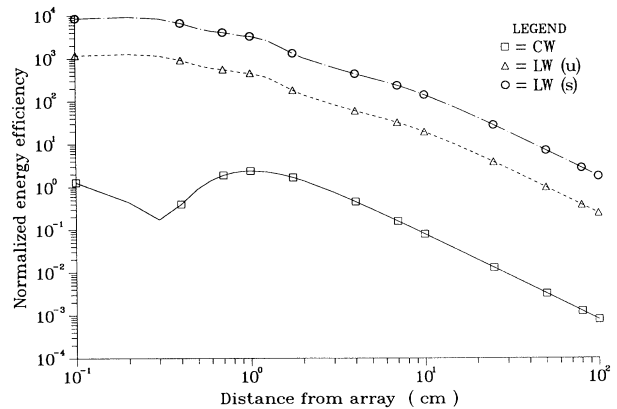


FIG. 7. Comparison of the decay of the measured-field energy along the line-of-sight direction of the beams generated by the LW and CW pulse-driven arrays.

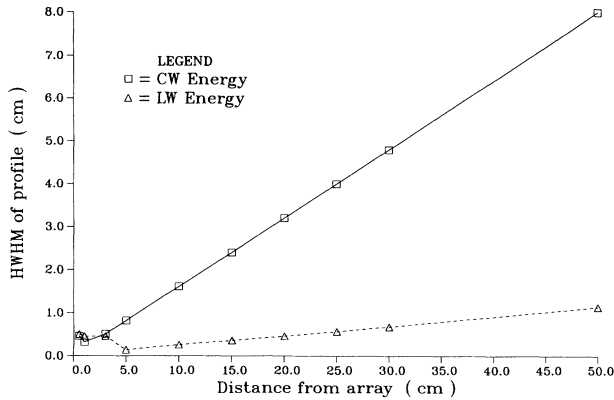


FIG. 8. Comparison of the expansion (half width at half maximum) along the line-of-sight direction of the measured-field-energy profiles of the beams generated by the LW and CW pulse-driven arrays.

expanding 2.03 and 3.66 times faster than their LW counterparts, and the LW radiated-beam-energy profile is expanding 1.77 times faster than its intensity profile. Similarly in Fig. 8 the waists of the CW and LW measured-field-energy profiles are given. The slopes of the CW and LW beam profiles are, respectively, 0.16 and 0.022. Thus the CW measured-beam-energy profile is expanding 7.26 times faster than the LW profile, which is also in reasonable agreement with the predicted value.

The numerical results summarized by Figs. 4–8 clearly demonstrate the improvements that are available from LW pulse-driven arrays. The measured LW beams can be made to be more efficient and narrower than their CW counterparts. Similarly, the radiated intensity of the beam generated by the LW pulse-driven array may be significantly higher than its CW counterpart. These beam enhancements have been confirmed experimentally [10]. The experimental value for the ratio between the measured LW and CW field energies was 6.0 instead of the value 12.11 predicted here; and the ratio of the LW and CW measured far-field intensities was approximately 12.21, more than double the energy enhancement. The LW measured-beam-energy profile was measured to be expanding 1.49 times faster than its intensity profile; it was expanding 4.25 times more slowly than the CW beam. Although the theoretical results indicate that further improvements are possible, these experimental results demonstrate the merit of the beams generated by a LW pulse-driven array.

C. Alternative LW pulse-driven arrays

Having demonstrated explicitly the advantages of a LW pulse-driven array over its CW counterpart, we can now consider modifications on those constructs or alternative concepts altogether. In particular, consider the folded array when the elements are taken closer to the origin. The resulting beams will have higher effective frequencies because signals are now being included which naturally have small amplitudes and large time variations (signals in the tails of the LW solution), but whose ampli-

tudes are amplified by the Jacobian term $(R_{\max}/\rho)^4$ in (3.19). This term rapidly becomes larger as ρ gets closer to the origin. On the other hand, the energy efficiency of the folded array may decrease because this same Jacobian term increases the input energy requirements. If efficiency were not an issue, one could develop a beam with an extremely narrow mainlobe but which wastes much of its energy in leakage to its tails. Such an example was discussed in Ref. [3] where the MPS pulse amplitude was maintained for many Rayleigh lengths but at a severe cost in efficiency. Another tentative example is discussed in Appendix B. One would gain in resolution at the cost of the beam's brightness. The usefulness of such a beam would, of course, depend on its intended application.

Consider again the CW pulse-driven array. The amplitudes of these signals are tapered (amplitude tapering or shading) across the array in practice to achieve a large reduction in sidelobe levels. This is accomplished with an acknowledged loss of beam directivity and a broadening of the mainlobe. The mainlobe can be made brighter with an increase in the frequency of the driving signal; however, without additional amplitude tapering, higher sidelobe levels will result. Eventually, if one were to raise the frequency of the driving signals to a value where the corresponding wavelength is smaller than the element separation, then the resultant CW beam will contain significant grating lobes. This is a particularly acute problem when the array is sparsely populated with elements. As noted above, the broad-bandwidth LW pulse-driven array can be designed to avoid this problem. This is illustrated in Fig. 9. The theoretical measured-field-beam-intensity profile for the folded MPS pulse-driven array considered in the preceding section is compared directly to the measured-field profiles of the beams generated by driving that array with CW tone bursts at 0.5 and 2.0 MHz. These curves were obtained in the plane $z = 30.0$ cm by searching the time history at a given radius and $z = 30.0$ cm for its maximum value and then plotting that value against its ρ value. The intensity profiles are all normalized to unity along the z axis. There are 101 data points in the profiles; ρ ranges from -50.0 to $+50.0$ cm. The wavelength at 0.5 MHz is 3.0 mm, slightly larger than the element spacing of 2.5 mm. On the other hand, at 2.0 MHz the wavelength is 0.75 mm, much smaller than the element spacing. As shown in Fig. 9, the broader beam profile of the 0.5-MHz case is traded for the narrower mainlobe and large grating lobes in the 2.0-MHz case. The folded-array beam has a main lobe similar to the higher-frequency CW case and sidelobe levels similar to the lower-frequency CW case. These qualities of the LW beam make it very appealing for a variety of applications.

Consider now the edge-enhanced array discussed at the beginning of this section. Although the analysis of this array is not yet complete, some preliminary statements can be made. The MPS pulse-driven array considered in Sec. III A was augmented with signals included in the elements located on the edge of the array. Those signals were defined by the appropriate boundary wave-diffraction terms obtained from the time version of the

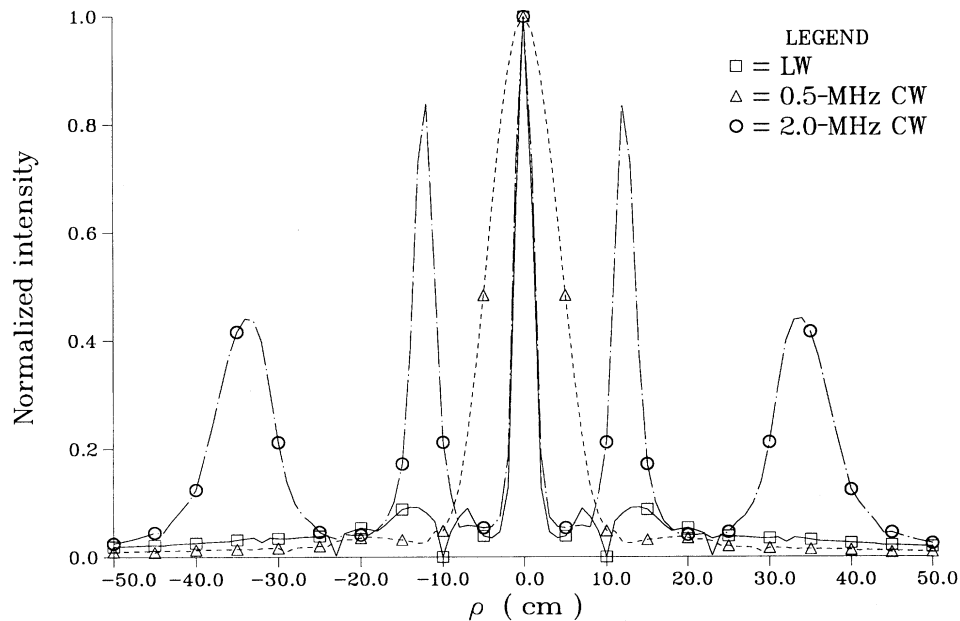


FIG. 9. Comparison of the normalized measured-field-intensity profiles at $z = 30.0$ cm of the beams generated by the LW and 0.5- and 2.0-MHz CW pulse-driven arrays.

corresponding Poincaré lemma derived explicitly by Miyamoto in Ref. [25]. This scheme has been crudely implemented numerically for the sparse 25-element square array considered above. The computational cost of obtaining the diffraction wave signals is quite high, so only a coarse signal set has been obtained to date. The resulting beam was found to have a narrower measured energy profile but a wider measured intensity profile than the corresponding folded-array beam. The associated energy efficiency was thus higher, while the intensity efficiency was lower. These results suggest that such a pulse-driven array may be useful in generating beams with further enhanced energy profiles. This concept is currently under further investigation.

IV. DISCUSSION

The possibility of generating LW beams from an array with diffraction lengths or near-field distances much larger than anticipated from conventional CW theory was addressed in this paper. This was accomplished by investigating and understanding the physics and engineering of driving arrays with a spatially distributed set of broad-bandwidth pulses. Bounds were derived that refine the meaning of a diffraction length and a diffraction-limited beam, particularly for those excitations. It was shown that one can design a set of driving signals for an array that can extend the near field further from an array with a more localized beam than is possible with a comparable CW system. The LW source-free solutions introduced in Ref. [3] were then used to illustrate such a set of designed pulses.

The utilization of an extended frequency set to drive the array introduces beam characteristics which result from different portions of the given frequency set. The

bounds presented in Sec. II were derived in terms of average and point quantities that characterize those frequency subsets. The enhanced localization properties and diffraction lengths of the resulting beams are closely connected with the existence of these additional frequency subsets which do not exist in the CW or narrow-band cases.

It was shown that several diffraction or Rayleigh lengths need to be introduced to describe the behavior of beams generated by pulse-driven arrays. Given the performance criterion, it was clearly demonstrated that LW beams outperform their CW counterparts. Diffraction-free beams with finite energy do not exist, as pointed out in Refs. [3] and [26]. However, the arguments presented here indicate that performance enhancements of array generated beams can be accomplished with frequency shading as well as amplitude shading of the array. If the transmitting and receiving arrays behave equally for all driving and received signals, the only control over the beam characteristics one has is through the driving functions. One must properly shape the frequency spectra of the input field to take into account the effects of the transmitting array and the measurement process. Beams *can* be generated from pulse-driven arrays that act as moving interference patterns with extended localization properties. The LW solutions simply provide an immediate access to these enhancements.

It was shown that there is an essential difference in the behavior of the radiated and measured fields for systems of transmitting and receiving elements that are and are not electrically large for the wavelengths of significance in the signals driving them. This difference was distinguished by a one- versus a three-time-derivative behavior of the output signals which resulted from the energy conversion processes at transmission and reception. It

led to the characterization of the radiated and measured fields, respectively, by the second- and sixth-order moments of the power spectra of the input signals. It was shown that a properly designed set of driving signals which have a high degree of correlation in the higher-order moments of their power spectra will produce a beam that has the desired extended diffraction lengths and enhanced localization properties. The diffraction process affects the higher-order moments of the spectra more slowly, giving the extended diffraction length; the enhanced transverse localization results from the high degree of correlation. Because they are simply related by powers of the frequency, there is essentially no difference between the radiated, propagated, and measured fields for a pulse-driven CW array. The broad-bandwidth LW signals can be tailored to the transmitter-receiver system configuration of interest to realize enhancements of a particular beam parameter.

Can these beam improvements be enhanced further? Since we are dealing only with linear phenomena, no new frequency content can be introduced into the resulting beams either by the transmitter, the medium, or the receiver than is present in the signals delivered to the array. However, as indicated, one can improve the results further still but within the context of introducing the appropriate diffraction lengths. Several possibilities exist as noted. Remaining efforts in this direction are truly of an engineering nature since they deal specifically with enhancing the beam quantities for particular applications. These include remote-sensing, communications, and directed-energy (sonar, radar) systems.

Nonetheless, significant physics issues remain, including the behavior of the broad-bandwidth LW beams under scattering and diffraction. Since many areas of physics deal with beams and those applications, the results presented here suggest that LW pulse-driven arrays may offer significant improvements over conventional CW systems in use today. Some of the remaining physics issues have been addressed recently. For instance, the propagation of a LW beam in a graded-layer-index medium and the scattering of a LW beam from an index discontinuity have been considered. The use of LW beams in remote-sensing problems is also currently under investigation both theoretically and experimentally. The results of both of these efforts have been very positive to date and will be reported elsewhere.

ACKNOWLEDGMENTS

The author is deeply indebted to D. Kent Lewis of the Advanced Ultrasonics Laboratory at the Lawrence Livermore National Laboratory for his many hours of time spent discussing these issues with me. The author also would like very much to thank Professor Ioannis M. Besieris of the Bradley Electrical Engineering Department at Virginia Polytechnic Institute and State University, Professor Donald Dudley and Professor Andreas Cangelaris of the Department of Electrical and Computer Engineering at the University of Arizona, and Dr. Kendall Casey of JAYCOR for their many useful suggestions concerning this work and this manuscript. This

work was performed in part by the Lawrence Livermore National Laboratory under the auspices of the U.S. Department of Energy under Contract No. W-7405-ENG-48.

APPENDIX A: ACOUSTIC-PIEZOELECTRIC-TRANSDUCER MODEL

The acoustic transducers used in the LW experiments [9,10] were of a common type which can be modeled simply as parallel-plate capacitors loaded with piezoelectric material. The faces of the piezoelectric material have an area A and the separation between the voltage contacts attached to these faces is l_z . It will be assumed, as was the actual case in the experiments [9,10], that the transducers are driven far from any of their (frequency) resonance points. The associated physical model is greatly simplified in this regime.

In its transmission mode the transducer material expands and contracts along the direction of the applied voltage signal launching a pressure wave; in the reciprocal reception mode an applied pressure wave deforms the piezoelectric material along this direction generating the measured voltage signal. In particular, the piezoelectric effect is expressed as a relationship $e = ps + Ed$ between the elastic strain e of the material and the electric field E and the pressure p applied to it, where d is the piezoelectric strain coefficient and s is the elastic compliance coefficient. If the stresses are applied in a uniform manner, then $e \sim 0$. Consequently, the pressure induced on the face of the transducer, hence in the medium, by an applied voltage signal is

$$p(t) \approx -\frac{d}{l_z s} v(t). \quad (\text{A1})$$

On the other hand, the voltage induced across the transducer by a pressure signal applied to its face is

$$v(t) \approx -\frac{l_z s}{d} p(t). \quad (\text{A2})$$

Consider one of these capacitive transducers in its transmission mode. Let the transducer be a disk with face area $A_T = \pi a^2$, a being its radius. The Fourier transform of the pressure field $\hat{P}(r, \theta, \phi, \omega)$ generated by such a transducer is given by the Rayleigh diffraction expression. When the observation point \mathbf{r} is in the far field of the transducer, i.e., the distance $r = |\mathbf{r}|$ from the center of the transducer to that point satisfies $r > A_T/\lambda$ over the frequency regime of interest, this pressure field has the form

$$\begin{aligned} \hat{P}(\mathbf{r}, \omega) &\sim -iZ_0 \left[\frac{\omega}{c} \right] [2A_T \hat{U}(\omega)] \frac{e^{ikr}}{4\pi r} \left[2 \frac{J_1(ka \sin\theta)}{(ka \sin\theta)} \right] \\ &\sim -iZ_0 \left[\frac{\omega}{c} \right] [2A_T \hat{U}(\omega)] \frac{e^{ikr}}{4\pi r}, \end{aligned}$$

where $\omega = kc$ is the frequency; $\hat{U}(\omega)$ is the Fourier transform of the velocity of the transducer face; c is the speed of sound in the medium; and $Z_0 = \rho_m c$ is the characteris-

tic impedance of the medium, ρ_m being its density. Since the angle θ between the transducer axis and the observation point is assumed small, the pattern term $[2J_1(x)/x]$ is set to unity. In the time domain this field becomes

$$p(\mathbf{r}, t) \sim \frac{Z_0 A_T}{2\pi r} \partial_{ct} u(t - r/c), \quad (\text{A3})$$

the face velocity being evaluated at the retarded time $t - r/c$.

Assuming the transducer is not electrically large, i.e., the frequencies of importance in the signal satisfy $\omega l_z/c = kl_z \lesssim 1$, the frequency-domain results given by Ristic (Ref. [27], pp. 153–157) relate the velocity of the face of the transducer $U(\omega)$ to the pressure $P(\omega)$ applied to the transducer face through the mechanical impedance: $U(\omega) = [Z_{\text{mech}}(\omega)]^{-1} P(\omega) \approx -i\omega l_z / (Z_0 c)$. Converting this result to the time domain yields

$$u(t) \approx \frac{l_z}{Z_0} \partial_{ct} p(t). \quad (\text{A4})$$

Combining this with (A1) gives

$$u(t) \approx -\frac{l_z}{Z_0} \frac{d}{l_z s} \partial_{ct} v_{\text{in}}(t) = -\frac{d}{Z_0 s} \partial_{ct} v_{\text{in}}(t). \quad (\text{A5})$$

Therefore the far-field pressure field (A3) can be written explicitly in terms of the input voltage signal;

$$p(\mathbf{r}, t) \approx -\frac{A_T}{2\pi r} \left[\frac{d}{s} \right] \partial_{ct}^2 v_{\text{in}}(t - r/c). \quad (\text{A6})$$

Now assume that this pressure field is measured with a matched (material) transducer with face area A_R . The output signal of this measurement is the voltage measured across a purely resistive impedance Z_R connected to the voltage plates on the transducer. Since this measurement occurs in the far field of the transmitter, the pressure field is essentially uniform across the face of the receiving transducer. Now when $kl_z \lesssim 1$, the transducer acts like a capacitor with capacitance $C_R = \epsilon A_R / l_z$ in this measurement circuit, ϵ being the permittivity of the piezoelectric material. Therefore with (A2) the output voltage signal is related to the voltage v_p induced across the transducer by the pressure field p as

$$\begin{aligned} v_R(t) &\approx Z_R i_R(t) \\ &= Z_R C_R \partial_t v_p(t) \\ &= -Z_R C_R \left[\frac{l_z s c}{d} \right] \partial_t p(t) = -\frac{Z_R}{Z_m} A_R \frac{s}{d} \partial_t p(t), \end{aligned} \quad (\text{A7})$$

where the impedance $Z_m^{-1} = \epsilon c$ has been introduced. With (A6) the measured voltage and the input voltage signals are related through the relation

$$v_R(t) \approx \frac{Z_R}{Z_m} \frac{A_R A_T}{2\pi r} \partial_{ct}^3 v_{\text{in}}(t - r/c), \quad (\text{A8})$$

which gives the anticipated three-time-derivative relationship. Introducing the constant $\mathcal{C} = (Z_R Z_0 / Z_m^2)^{1/2} (A_T A_R)^{1/2} / c^2$ and the functions $f(t) = v_{\text{in}}(t) / (A_T Z_0)^{1/2}$ and $g(t) = v_R(t) / (A_R Z_R)^{1/2}$, the received signal can then be written in the anticipated canonical form:

$$g(t) \approx \mathcal{C} \frac{A_T}{2\pi c r} \partial_{ct}^3 f(t - r/c), \quad (\text{A9})$$

where the constant \mathcal{C} , the input signal f , and the output signal g have, respectively, the units s^2 , $(\text{W}/\text{m}^2)^{1/2}$, and $(\text{W}/\text{m}^2)^{1/2}$.

APPENDIX B: AMPLITUDE MAINTENANCE FROM A MPS PULSE-DRIVEN APERTURE

Consider an aperture that is driven with the MPS pulse. In the far field, the Huygens representation (2.2) can be rewritten in the form

$$\begin{aligned} g(\mathbf{r}, t) &\sim \int_{A_n} dS' \frac{1}{4\pi R} (-[\partial_z f] + [\partial_{ct} f]) \\ &= -\int_{A_n} dS' \frac{1}{2\pi R} [\partial_\tau f], \end{aligned} \quad (\text{B1})$$

where $\tau = z - ct$. To examine the distance over which the initial field amplitude is recovered from a circular aperture of radius R_a driven with a MPS pulse, one can insert the bidirectional representation of the axisymmetric LW pulses given in Ref. [4],

$$\begin{aligned} \Psi(\rho, z, t) &= \text{Re} \frac{1}{(2\pi)^2} \int_0^\infty d\xi \int_0^\infty d\chi \frac{\chi}{\xi} C_0 \left[\frac{\chi^2}{4\xi}, \xi, \chi \right] J_0(\chi\rho) \\ &\quad \times e^{i\xi(z+ct)} \\ &\quad \times e^{-i(\chi^2/4\xi)(z-ct)}, \end{aligned} \quad (\text{B2})$$

into (B1) to obtain the expression for the field along the z axis,

$$g(\rho=0, z, t) \sim \text{Re} \frac{i}{4(2\pi)^2} \int_0^\infty d\xi \int_0^\infty d\chi \frac{\chi^3}{\xi^2} C_0 \left[\frac{\chi^2}{4\xi}, \xi, \chi \right] e^{i\xi(z+ct)} e^{-i(\chi^2/4\xi)(z-ct)} \Pi(z, z'; \chi, \xi). \quad (\text{B3})$$

Note that the MPS pulse used in the simulations and experiments is taken to be the real part of the expression resulting from the bidirectional representation, this operation being represented by the symbol Re . The integral

$$\Pi(z, z'; \chi, \xi) = \int_0^{R_a} d\rho' \rho' \frac{J_0(\chi\rho')}{R} e^{-i(\xi + \chi^2/4\xi)R_a} \quad (\text{B4})$$

contains the z dependence of the aperture-generated far field. Its approximate evaluation is straightforward assuming $R_a \ll (z - z')$ so that one can employ the usual constructions for the timing and attenuation factors. One obtains a canonical diffraction integral defined by the Lommel functions. In particular, if $\Lambda = [\xi/2(z - z')](1 + \chi^2/4\xi^2)$, then [28]

$$\begin{aligned} \Pi(z, z'; \chi, \xi) &\sim \frac{e^{-i(\xi + \chi^2/4\xi)(z - z')}}{z - z'} \int_0^{R_a} d\rho \rho J_0(\chi\rho) e^{-i[(\xi + \chi^2/4\xi)/2(z - z')]\rho^2} \\ &= \frac{e^{-i(\xi + \chi^2/4\xi)(z - z')}}{z - z'} \frac{e^{-i[(\xi + \chi^2/4\xi)/2(z - z')]R_a^2}}{2\Lambda} [U_1(2\Lambda R_a^2, \chi R_a) + iU_2(2\Lambda R_a^2, \chi R_a)], \end{aligned} \quad (\text{B5})$$

where the Lommel functions are given by

$$U_n(x, y) = \sum_{k=0}^{\infty} \left[\frac{x}{y} \right]^{2k+n} J_{2k+n}(y). \quad (\text{B6})$$

This expression can be reduced further depending, of course, on the behavior of C_0 .

The bidirectional spectrum [4] C_0 of the normalized MPS pulse for $\alpha = 1.0$ that we have considered here is

$$C_0(u, v, \chi) = 2\pi^2 \beta z_0 a H \left[v - \frac{b}{\beta} \right] e^{-[uz_0 + (\beta v - b)a]}, \quad (\text{B7})$$

where $H(x)$ is the Heaviside function. Because of the exponential decay behavior for large u or large v , the coefficients of the Bessel terms in the Lommel functions in (B5) are always very small: $2\Lambda R_a^2/(\chi R_a) = (\xi/\chi + \chi/\xi)[R_a/(z - z')] \ll 1$, hence the expression (B5) can be reduced to the form

$$\Pi_{\text{MPS}}(z, z'; \chi, \xi) \sim \frac{e^{-i(\xi + \chi^2/4\xi)(z - z')}}{z - z'} \frac{e^{-i[(\xi + \chi^2/4\xi)/2(z - z')]R_a^2}}{\chi} R_a J_1(\chi R_a). \quad (\text{B8})$$

One would expect the amplitude of the field to take on its maximum value at or near the pulse center $z = z' + ct$. Evaluating the far-field expression (B3) at this point and using (B8), one obtains

$$\begin{aligned} g(\rho=0, z, t=(z - z')/c) &\sim -\text{Re}(\beta z_0 a) \frac{i}{8} \frac{R_a}{z - z'} \int_{b/\beta}^{\infty} d\xi \frac{1}{\xi^2} e^{i\xi[z' - R_a^2/2(z - z')]} e^{-(\beta\xi - b)a} \\ &\quad \times \int_0^{\infty} d\chi \chi^2 J_1(\chi R_a) e^{-i\chi^2 \Gamma(\xi, z - z')}, \end{aligned} \quad (\text{B9})$$

where the term

$$\Gamma(\xi, z - z') = \frac{1}{4\xi} \left[z_0 + iz' + i \frac{R_a}{2(z - z')} \right] \equiv \frac{1}{4\xi} \Omega(z - z').$$

The χ integration can be performed with the identity [Ref. [29], Eq. (6.631.4), p. 717]

$$\int_0^{\infty} d\chi \chi^2 J_1(\chi R) e^{-\Gamma\chi^2} = \frac{R}{(2\Gamma)^2} e^{-R^2/4\Gamma}.$$

This means

$$g(\rho=0, z, t=(z - z')/c) \sim -\text{Re} \frac{i}{2} \frac{R_a^2}{z - z'} \frac{\beta z_0 a}{\Omega^2} e^{ba} \int_{b/\beta}^{\infty} d\xi e^{-\xi\{\beta a + R_a^2/\Omega - i[z' - R_a^2/2(z - z')]\}}. \quad (\text{B10})$$

Since

$$\int_u^{\infty} dx e^{-\eta x} = \frac{e^{-\eta u}}{\eta},$$

the ξ integration is straightforward and yields, for $\beta a \gg 1$,

$$\begin{aligned} g(\rho=0, z, t=(z - z')/c) &\sim -\text{Re} \frac{i}{2} \frac{R_a^2}{\Omega^2} \frac{\beta z_0 a}{(z - z')} \frac{e^{i(b/\beta)[z' - R_a^2/2(z - z')]} e^{-(b/\beta)(R_a^2/\Omega)}}{\beta a + R_a^2/\Omega - i[z' - R_a^2/2(z - z')]} \\ &\sim -\text{Re} \frac{i}{2} \frac{R_a^2}{\Omega^2} \frac{z_0}{(z - z')} e^{i(b/\beta)[z' - R_a^2/2(z - z')]} e^{-(b/\beta)(R_a^2/\Omega)}. \end{aligned} \quad (\text{B11})$$

Introducing the Rayleigh distance $L_R = R_a^2/(2z_0) = \pi R_a^2/\lambda_{\min}$ and taking (without loss of generality) $z' = 0$, one finds that

$$\begin{aligned}
|\Omega|^2 &= z_0^2 [1 + (L_R/z)^2], \\
\frac{1}{\Omega} &= \frac{1}{z_0 [1 + (L_R/z)^2]} [1 - i(L_R/z)], \\
|\Omega^2|^2 &= z_0^4 \{ [1 - (L_R/z)^2]^2 + 4(L_R/z)^2 \} = z_0^4 [1 + (L_R/z)^2]^2, \\
\frac{1}{\Omega^2} &= \frac{1}{z_0^2 [1 + (L_R/z)^2]^2} \{ [1 - (L_R/z)^2] - 2i(L_R/z) \},
\end{aligned}$$

which allows one to rewrite (B11) in the form

$$g(\rho=0, z, t=z/c) \sim \frac{L_R}{z} \left[\frac{[1 - (L_R/z)^2]}{[1 + (L_R/z)^2]^2} \sin\psi - \frac{2(L_R/z)}{[1 + (L_R/z)^2]^2} \cos\psi \right] e^{-2(b/\beta)L_R/[1 + (L_R/z)^2]}, \quad (\text{B12})$$

where the phase

$$\psi = (b/\beta) \left[\frac{2L_R^2}{z[1 + (L_R/z)^2]} - z_0 \frac{L_R}{z} \right].$$

From (B12) one sees that if $z \gg L_R$, then g decays as $1/z^2$, faster than $1/z$. On the other hand, if $z \ll L_R$ and $z \gg R_a$, then $g \sim -z/L_R$ which is growing monotonically with z . Therefore, to establish the diffraction length, one must consider the region where $R_a < z < L_R$. In this region $\psi \sim 2(b/\beta)z$ and

$$g(\rho=0, z, t=z/c) \sim -\frac{z}{L_R} \left[\sin \left[2 \frac{b}{\beta} z \right] + 2 \left[\frac{z}{L_R} \right] \cos \left[2 \frac{b}{\beta} z \right] \right] e^{-2(b/\beta)z^2/L_R}. \quad (\text{B13})$$

One thus finds that the field on the axis of the array varies as $g \sim x \exp(-\alpha x^2)$ where $x = z/L_R$ and $\alpha = 2(b/\beta)L_R$. This means that $g \sim \frac{1}{2}$ when $\ln x - \alpha x^2 = \ln \frac{1}{2}$ or when $x \sim [-\ln(\frac{1}{2})/\alpha]$. For a circular aperture of radius R_a driven with a MPS pulse whose waist $w^2 = \beta z_0/b$ and minimum wavelength $\lambda_{\min} = 2\pi z_0$, the associated diffraction length is the z value:

$$z_R \sim \left[\frac{\beta}{4b} L_R \right]^{1/2} = \left[\frac{\beta}{bz_0} \right]^{1/2} \frac{R_a}{2} = \frac{wR_a}{2z_0} \equiv \frac{\pi w R_a}{\lambda_{\min}} = \left[\frac{R_a}{w} \right] L_G. \quad (\text{B14})$$

Thus the diffraction length of the MPS pulse-driven aperture is greater than $L_G = \pi w^2/\lambda_{\min}$, the diffraction length associated with that aperture driven by a CW (monochromatic) Gaussian beam with frequency c/λ_{\min} and initial waist $w_0 = w$. Note that $z_R \leq L_R$, the diffraction length associated with driving the *entire* aperture uniformly with the same CW signal at the frequency c/λ_{\min} .

A natural question of course arises as to whether the MPS pulse-driven aperture case is or is not the optimal case for achieving the maximum distance of amplitude maintenance from a fixed aperture size. Clearly it is not. The folded MPS array case outperforms the simpler unfolded one. What then is the optimal LW pulse? Unfortunately, it is not known explicitly at this time. Reconsider now Eqs. (B3) and (B8). One has a large latitude for the choice of the LW pulse (bidirectional) spectrum $C_0(u, v, \chi)$. Instead of the MPS spectrum, let us tailor a spectrum for the given aperture. In particular, set

$$C_0(u, v, \chi) = \pi^2 a_1 a_2 \frac{e^{-a_1 u} e^{-a_2 v}}{u v} \frac{\chi R_a}{J_1(\chi R_a)}. \quad (\text{B15})$$

With this bidirectional spectrum the field

$$\begin{aligned}
g(\rho=0, z, t=(z-z')/c) &\approx \frac{i}{(2\pi)^2} \frac{R_a}{(z-z')} \int_0^\infty d\xi e^{i\xi[z' - R_a^2/2(z-z')]} \\
&\quad \times \int_0^\infty d\chi \frac{\chi^2}{4\xi^2} C_0 \left[\frac{\chi^2}{4\xi}, \xi, \chi \right] J_1(\chi R_a) e^{-(\chi^2/4\xi)[z' + R_a^2/2(z-z')]} \\
&= \frac{i}{4} \frac{a_1 a_2 R_a^2}{(z-z')} \int_0^\infty d\xi \frac{1}{\xi} e^{-\xi\{a_2 - i[z' - R_a^2/2(z-z')]\}} \int_0^\infty d\chi \chi e^{-\chi^2\{a_1 + i[z' + R_a^2/2(z-z')]\}/4\xi} \\
&= \frac{ia_1 a_2 R_a^2}{2(z-z')} \left[\frac{1}{a_1 + i[z' + R_a^2/2(z-z')]} \right] \int_0^\infty d\xi e^{-\xi\{a_2 - i[z' - R_a^2/2(z-z')]\}} \\
&= \frac{i}{2} \frac{a_1 a_2 R_a^2}{2(z-z')} \left[\frac{1}{a_1 + i[z' + R_a^2/2(z-z')]} \right] \left[\frac{1}{a_2 - i[z' - R_a^2/2(z-z')]} \right], \quad (\text{B16})
\end{aligned}$$

which $\sim a_2$ or $\sim a_1$, depending upon whether $(z-z') \ll R_a^2/a_2$ and $R_a^2/a_1 \ll (z-z')$ or $(z-z') \ll R_a^2/a_1$ and $R_a^2/a_2 \ll (z-z')$. In analogy with the MPS pulse case, it is believed that the constant a_1 controls the maximum frequency ($\omega_{\max} \sim c/a_1$) and a_2 controls the distance of pulse shape maintenance so that one would choose a desired frequency regime by choosing an appropriate a_1 and then set $a_2 \ll a_1$ to achieve $g \sim a_2$ and a radiated intensity diffraction length $L_{\text{rad}}^{\text{int}} \sim \pi R_a^2/a_2 \gg \pi R_a^2/a_1$. Note that the constants a_1 and a_2 can, of course, be factored from the spectrum (B15) to give $g \sim 1$ at $t = (z-z')/c$ in (B16). The spectrum (B15) does not lend itself to an analytical determination of the corresponding LW solution. We are currently trying to determine the form of this solution numerically. Once this is accomplished, the associated effective frequencies can be obtained; and the propagation simulator can be used to investigate the characteristics of the beam generated by driving an array with this LW solution.

APPENDIX C: AMPLITUDE MAINTENANCE FROM A UNIFORM, CW-TONE-BURST PULSE-DRIVEN APERTURE

Consider the field generated from a uniform, CW-driven aperture of radius R_a . With the Huygens representation, if the array is driven with the tone burst $g(t) = \sin \omega t [H(t) - H(t - T_{\text{off}})]$, where $T_{\text{off}} = n(2\pi/\omega)$, it generates the field

$$\begin{aligned} f(\rho, z, t) &= - \int_S \frac{1}{4\pi R} \left[\partial_z g(t - R/c) - \partial_{ct} g(t - R/c) \frac{z-z'}{R} - g(t - R/c) \frac{z-z'}{R^2} \right] \\ &= \int_S \frac{1}{4\pi R} \left[\frac{\omega}{c} \frac{z-z'}{R} \cos[\omega(t - R/c)] + \frac{z-z'}{R^2} \sin[\omega(t - R/c)] \right] \\ &\quad \times [H(t - R/c) - H(t - R/c - T_{\text{off}})], \end{aligned} \quad (\text{C1})$$

where $R = [(x-x')^2 + (y-y')^2 + (z-z')^2]^{1/2}$. We take the time T_{off} the tone burst exists to be a multiple of the period to avoid the discontinuities that occur at the final end point when the time derivative in (C1) is applied to the driving function $g(t)$.

We consider specifically a circular aperture of radius a and confine the observation points to those along the direction of propagation. If we make the change of variables $u = ct - R$ and set $\Gamma = [R_a^2 + (z-z')^2]^{1/2}$, (C1) gives

$$\begin{aligned} f(\rho=0, z, t) &= \frac{z-z'}{2} \int_0^{R_a} d\rho \rho \left[\frac{\omega}{c} \frac{\cos[\omega(t - R/c)]}{R^2} + \frac{\sin[\omega(t - R/c)]}{R^3} \right] [H(t - R/c) - H(t - R/c - T_{\text{off}})] \\ &= - \frac{z-z'}{2} \left[\frac{\omega}{c} \int_{ct-(z-z')}^{ct-\Gamma} du \frac{\cos(\omega/c)u}{ct-u} [H(u) - H(u - T_{\text{off}})] \right. \\ &\quad \left. + \int_{ct-(z-z')}^{ct-\Gamma} du \frac{\sin(\omega/c)u}{(ct-u)^2} [H(u) - H(u - T_{\text{off}})] \right]. \end{aligned} \quad (\text{C2})$$

With (Eq. (2.641.3), p. 187, Ref. [29]) the axial field expression (C2) becomes

$$\begin{aligned} f(\rho=0, z, t) &= \frac{z-z'}{2} \left[\frac{\sin\{(\omega/c)[ct - (z-z')]\}}{z-z'} [H(ct - (z-z')) - H(ct - (z-z') - cT_{\text{off}})] \right. \\ &\quad \left. - \frac{\sin[(\omega/c)(ct - \Gamma)]}{\Gamma} [H(ct - \Gamma) - H(ct - \Gamma - cT_{\text{off}})] \right]. \end{aligned} \quad (\text{C3})$$

We take the observation time to be relative to the time for a signal from the center of the array to reach the observation point $t = (z-z')/c + T_{\text{obs}}$. This simplifies (C3):

$$\begin{aligned} f(\rho=0, z, T_{\text{obs}}) &= \frac{z-z'}{2} \left[\frac{\sin[(\omega/c)cT_{\text{obs}}]}{z-z'} [1 - H(T_{\text{obs}} - T_{\text{off}})] \right. \\ &\quad \left. - \frac{\sin\{(\omega/c)[(z-z') - \Gamma + cT_{\text{obs}}]\}}{\Gamma} [H((z-z') - \Gamma + cT_{\text{obs}}) \right. \\ &\quad \left. - H((z-z') - \Gamma + cT_{\text{obs}} - cT_{\text{off}})] \right]. \end{aligned} \quad (\text{C4})$$

Let the distance from the array be much larger than the size of the array $z-z' \gg R^2$ so that $\Gamma \sim z-z'$. Also let the tone burst last one period and take the observation time to be less than the period: $T_{\text{obs}} < T_{\text{off}}$. The axial field then reduces to the form

$$\begin{aligned}
 f(\rho=0, z, T_{\text{obs}}) &= \frac{1}{2} \left\{ \sin \left[\frac{\omega}{c} (cT_{\text{obs}}) \right] + \sin \left[\frac{\omega}{c} \left[\frac{R_a^2}{2(z-z')} - cT_{\text{obs}} \right] \right] \right\} \\
 &= \sin \left[\frac{\omega}{c} \left[\frac{R_a^2}{4(z-z')} \right] \right] \cos \left[\frac{\omega}{c} \left[\frac{R_a^2}{4(z-z')} - cT_{\text{obs}} \right] \right]. \quad (\text{C5})
 \end{aligned}$$

We evaluate this expression at the peak of the driving function, i.e., at $T_{\text{obs}} = (2\pi/\omega)/4$. One obtains as a function of the distance from the array

$$f(\rho=0, z, T_{\text{obs}}) \approx \sin \left[\frac{\pi R_a^2}{2\lambda(z-z')} \right], \quad (\text{C6})$$

where use has been made of the free-space identity

$\omega/c = 2\pi/\lambda$. This result gives the conventional Fresnel integral oscillations if the distance constraint $(z-z') \ll R_a^2/\lambda$ is satisfied. The field obtains its last maximum at $(z-z') = R_a^2/\lambda$; it has decayed to 0.48, approximately its half-amplitude point, at $(z-z') = \pi R_a^2/\lambda = L_R$, the classical Rayleigh distance. The field then decays as $1/z$ for $z > L_R$ (in the far field).

*Previous address: University of California, Lawrence Livermore National Laboratory, Livermore, CA 94550.

- [1] J. B. Brittingham, *J. Appl. Phys.* **54**, 1179 (1983).
 [2] R. W. Ziolkowski, *J. Math. Phys.* **26**, 861 (1985).
 [3] R. W. Ziolkowski, *Phys. Rev. A* **39**, 2005 (1989).
 [4] A. M. Shaarawi, I. B. Besieris, and R. W. Ziolkowski, *J. Math. Phys.* **30**, 1254 (1989).
 [5] P. D. Einziger and S. Raz, *J. Opt. Soc. Am. A* **4**, 3 (1987).
 [6] E. Heyman and L. B. Felsen, *J. Opt. Soc. Am. A* **6**, 806 (1989).
 [7] P. Hillion, *J. Math. Phys.* **28**, 1743 (1987).
 [8] A. M. Shaarawi, I. M. Besieris, and R. W. Ziolkowski, *J. Math. Phys.* **31**, 2511 (1990).
 [9] R. W. Ziolkowski, D. K. Lewis, and B. D. Cook, *Phys. Rev. Lett.* **62**, 147 (1989).
 [10] R. W. Ziolkowski and D. K. Lewis, *J. Appl. Phys.* **68**, 6083 (1990).
 [11] M. Johnson, Lawrence Livermore National Laboratory, Report No. UCID-21661, 1989 (unpublished).
 [12] W. Burdic (private communication).
 [13] R. W. Ziolkowski (unpublished).
 [14] J. Hernandez, R. W. Ziolkowski, and S. Parker (unpublished).
 [15] B. D. Cook and D. K. Lewis, *Proc. Ultrasonics International 87* (Butterworth, London, 1987), p. 947.
 [16] D. S. Jones, *The Theory of Electromagnetism* (Pergamon, New York, 1964), pp. 38–42.
 [17] I. Stakgold, *Green's Functions and Boundary Value Problems* (Wiley, New York, 1979), pp. 270–272.
 [18] A. Siegman, *Lasers* (University Science Books, Mill Valley, CA 1986), p. 672.
 [19] T. T. Wu, *J. Appl. Phys.* **57**, 2370 (1985).
 [20] R. Chengli and W. Changhua, *Electron. Lett.* **25**, 1321 (1989).
 [21] R. W. Ziolkowski and G. A. Deschamps, *SIAM J. Math. Anal.* **15**, 535 (1984).
 [22] K. Miyamoto and E. Wolf, *J. Opt. Soc. Am.* **52**, 615 (1962); **52**, 626 (1962).
 [23] W. B. Gordon, *J. Math. Phys.* **16**, 448 (1975).
 [24] D. Lager and S. Azevedo, LLNL Report No. UCID-19912, Rev. 1, 1985 (unpublished).
 [25] K. Miyamoto, *Proc. Phys. Soc. London* **79**, 617 (1962).
 [26] T. T. Wu and H. Lehman, *J. Appl. Phys.* **60**, 2981 (1986).
 [27] V. Ristic, *Principles of Acoustic Devices* (Wiley, New York, 1983).
 [28] A. P. Prudnikov, Yu. A. Brunchkov, and O. I. Marichev, *Integrals and Series Volume 2: Special Functions* (Gordon and Breach, New York, 1986).
 [29] *Tables of Integrals, Series, and Products*, edited by I. S. Gradshteyn and I. M. Ryzhik (Academic, New York, 1965).